PG
Petroleum Geoscience

Research article

https://doi.org/10.1144/petgeo2022-036 | Vol. 28 | 2022 | petgeo2022-036

Structural characterization and across-fault seal assessment of the Aurora CO_2 storage site, northern North Sea

Nora Holden[1]*, Johnathon L. Osmond[1], Mark J. Mulrooney[1], Alvar Braathen[1], Elin Skurtveit[1,2] and Anja Sundal[1]

[1] Department of Geosciences, University of Oslo (UiO), PO Box 1047, Blindern, 0316 Oslo, Norway
[2] Norwegian Geotechnical Institute (NGI), PO Box Ullevål Stadion, 0806 Oslo, Norway
NH, 0000-0001-5846-5642
* Correspondence: nora.holden@geo.uio.no

Abstract: Faults play an essential role at many potential CO_2 storage sites because they can act as conduits or barriers to fluid flow. To contribute to the evaluation of the Aurora storage site in the northern North Sea, we perform a structural characterization and assessment of across-fault seals that displace the Lower Jurassic storage complex. We find that first-order faults are predominately north–south striking and west dipping, with throws greater than the thickness of the primary seal (>85 m). In contrast, second-order faults have lower throws (15–50 m), and variable strike and dip directions. Due to the dip of the storage complex, injected CO_2 is likely to migrate northwards before encountering the first-order Svartalv Fault Zone on its footwall side, which juxtaposes the storage units against younger sand-rich units. However, shale gouge ratio values exceed 0.30 at the depth of the storage complex, suggesting that a fault membrane seal may be present. Furthermore, second-order NE-dipping faults create juxtaposition seals and, in places, small-scale structural traps (24–48 m) along the Svartalv Fault Zone. Overall, we suggest that faults within the Aurora storage site could provide barriers to plume migration, allowing more CO_2 to become trapped and thereby increasing the storage capacity.

Thematic collection: This article is part of the Energy Geoscience Series available at https://www.lyellcollection.org/cc/energy-geoscience-series

Received 30 April 2022; **revised** 15 August 2022; **accepted** 31 August 2022

Carbon capture and storage (CCS) is considered one of the key technologies needed to meet the 1.5°C target set by the Paris Agreement and to achieve net zero emissions from the energy sector by 2050 (IPCC 2018; IEA 2021). Norway, as a frontrunner on this technology, has implemented CCS since 1996 at the Sleipner gas field in the North Sea (Torp and Gale 2004; Arts *et al*. 2008) and since 2008 at the Snøhvit gas field in the Barents Sea (Arts *et al*. 2008). Drawing from this experience, Norway is planning a new full-chain CCS operation by 2024. The Norwegian Government has named the project Longship, which will contribute to the development of carbon capture, transport and storage technologies (NMPE 2020).

In the first phases of Longship, CO_2 will be captured at the Norcem AS cement factory and Hafslund Oslo Celsio incineration plant, transported by ships to a new receiving terminal (Naturgassparken) in the municipality of Øygarden, and injected into saline sandstone aquifers roughly 2.7 km below sea level (Furre *et al*. 2020). The current location for subsurface storage is called Aurora and it resides within Exploitation Licence EL001 in the northern Horda Platform (Fig. 1a, b). The transport and storage aspect of Longship will be operated by the Northern Lights Joint Venture (i.e. Northern Lights JV DA), which is an industry-driven collaboration between Equinor ASA, A/S Norske Shell and Total E&P Norge AS (Gassnova 2020; Equinor ASA 2021). At Aurora, 1.5 Mt of supercritical CO_2 per year is planned to be injected over 25 years, with the aim of expanding this by an additional 3.5 Mt of CO_2 per year or more.

In 2019, the Northern Lights project drilled well 31/5-7 (also referred to as the Eos well) as a dedicated confirmation well for CO_2 storage, which verified the presence of a suitable storage complex (i.e. storage and seal units) within the Lower Jurassic Dunlin Group (Figs 1b and 2) (Vollset and Doré 1984; Marjanac and Steel 1997). More specifically, the sandstones of the Johansen and Cook formations form primary and secondary storage units, respectively (Furre *et al*. 2019; Furre *et al*. 2020), whereas overlying mudstones and shales of the Drake Formation form the envisaged primary seal (Furre *et al*. 2020; Osmond *et al*. 2022). Marine siltstones of the Upper Amundsen Formation (UAF; Burton Formation equivalent: Marjanac and Steel 1997) are present between the Johansen and Cook formations (Fig. 2); however, it lacks lateral continuity and is therefore not considered a regional seal for CO_2 storage (Sundal *et al*. 2016). The Draupne Formation, Cromer Knoll Group, Shetland Group and Rogaland Group are considered the secondary seal for storage in the Aurora CO_2 storage site (Furre *et al*. 2020).

The Lower Jurassic storage complex within the Aurora storage site dips towards the south, and, consequently, CO_2 is expected to migrate northwards and towards the Troll licence over time (Fig. 1b) (Furre *et al*. 2019; Furre *et al*. 2020). Towards the north, the large-scale basement-involved Svartalv Fault Zone and numerous, smaller-scale, basement-detached faults are present (Fig. 1b). Faults play a crucial role in proposed CO_2 storage sites as they can form both barriers and conduits to fluid flow (e.g. Watts 1987; Bjørlykke 1993; Knott 1993), thus affecting the migration pathways and the trapping of injected CO_2. Therefore, to ensure efficient storage, it is essential to assess how faults will influence the migration of CO_2. Previous publications have focused on the presence of fault seals below the Troll oil and gas field (Bretan *et al*. 2011; Bretan 2017), the prospective Smeaheia CO_2 storage area (Mulrooney *et al*. 2020; Wu *et al*. 2021), and regionally across the northern Horda Platform (Osmond *et al*. 2022). However, to date, no detailed assessments of across-fault seals and the structural character of faults within the proposed Aurora storage site have been published.

To address this, we created a detailed structural geomodel of the storage complex and intersecting faults within the Aurora storage

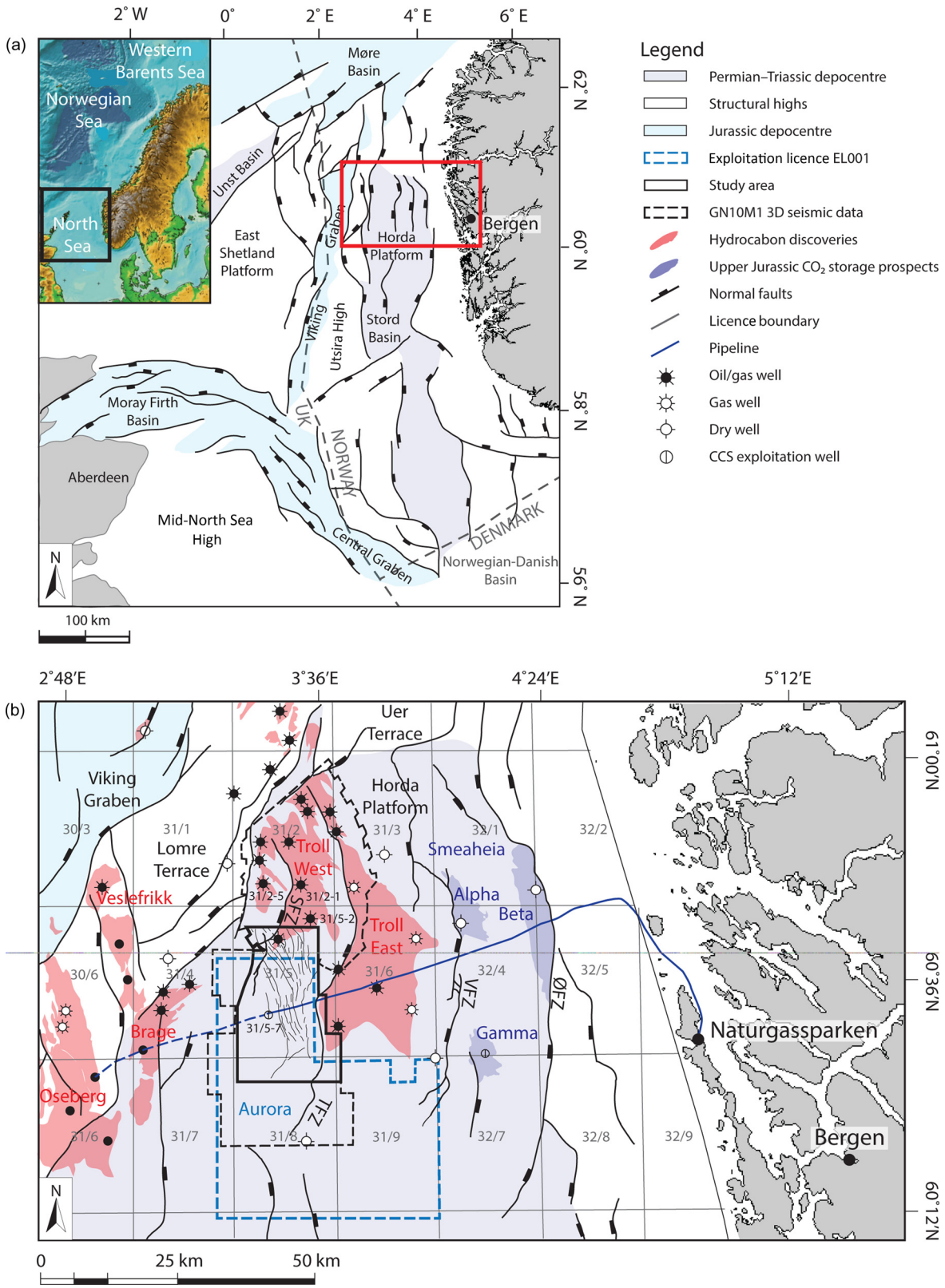

Fig. 1. Overview maps of structural elements in (**a**) the North Sea and (**b**) the northern Horda Platform. The red outline in (a) shows the location of the map in (b). The inset in (a) is modified from Faleide *et al.* (2010) and the structural element map is modified from Roberts *et al.* (1995). (b) The outline of structural elements in the Horda Platform is shown together with the outline of exploitation licence EL001, hydrocarbon discoveries, Upper Jurassic CO_2 storage prospects in the Smeaheia region, the GN10M1 merged 3D seismic survey and the study area applied in our work. The outlines of hydrocarbon discoveries, structural elements and well locations were compiled from the NPD FactMaps (2020), NPD FactPages (2020), and CO_2 storage prospects from Mulrooney *et al.* (2020) and Osmond *et al.* (2022). Note that not all existing wells have been included in the map. ØFC, Øygarden Fault Complex; VFZ, Vette Fault Zone; TFZ, Tusse Fault Zone; SFZ, Svartalv Fault Zone.

site by analysing and combining several data: the GN10M1 3D seismic survey, regional 2D seismic lines and well data. We present a detailed assessment of fault geometries and two types of across-fault seals: (i) juxtaposition seals (Allan 1989) and (ii) membrane seals (Watts 1987; Fisher and Knipe 2001) – using the shale gouge ratio (SGR) and shale smear factor (SSF) method

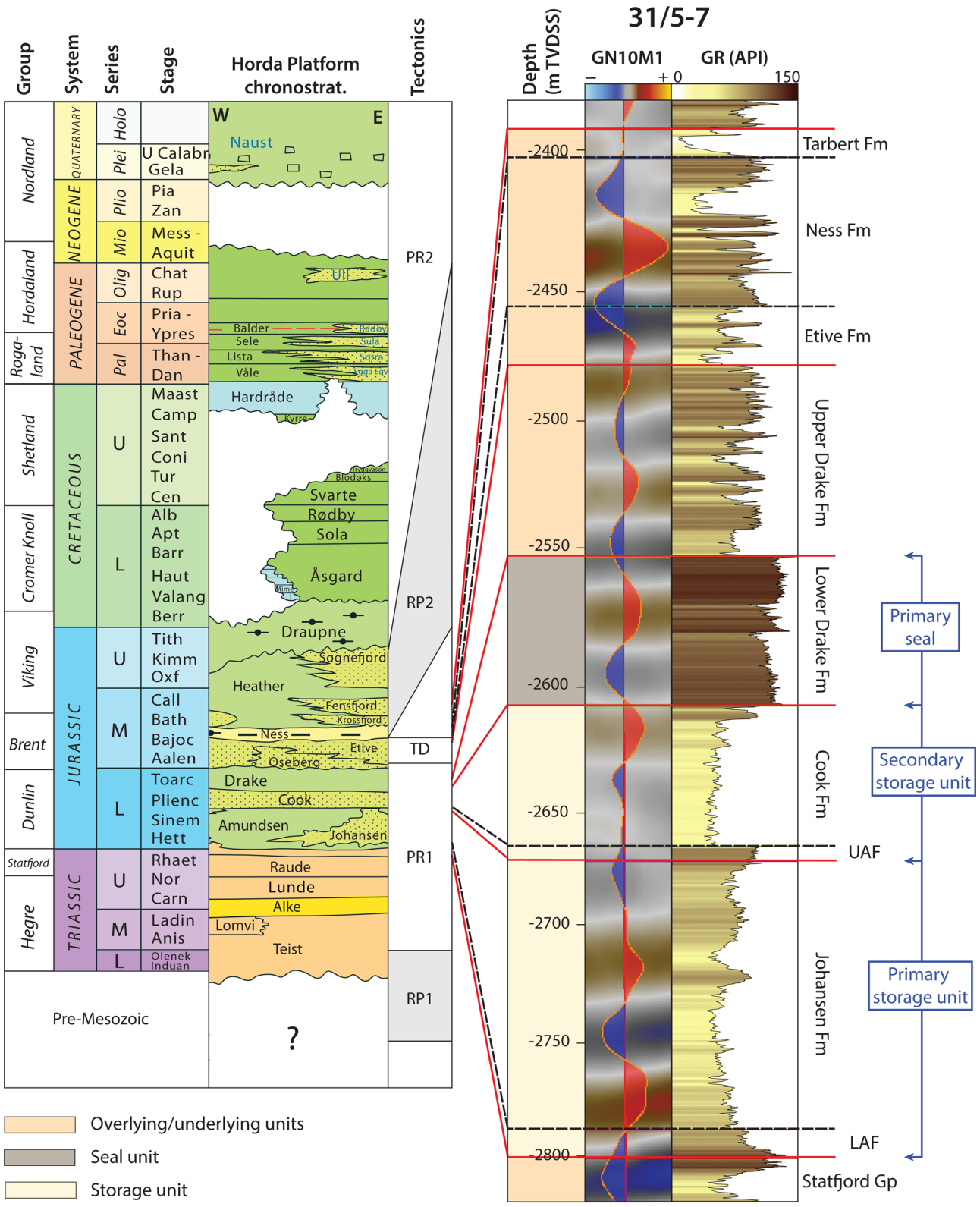

Fig. 2. A chronostratigraphic chart is shown together with major tectonic events in the northern North Sea. Key stratigraphic units representing the potential Lower Jurassic storage units (i.e. primary and secondary storage units) and the primary seal unit are marked by tops shown in the gamma-ray (GR) log from well 31/5-7 (Eos). A seismic section from GN10M1 is displayed together with a synthetic seismogram created using log data from well 31/5-7. Interpreted reflectors from this article are highlighted with red lines, whereas other reflectors are highlighted with black dashed lines. The chronostratigraphic chart is modified after NPD (2014), and Permian–Triassic (RP1) and Middle Jurassic–Early Cretaceous (RP2) tectonic events are compiled from Whipp *et al.* (2014) and Bell *et al.* (2014). Well data from 31/5-7 and the location of formation tops are courtesy of the Northern Lights project (Equinor ASA, Total E&P Norge and A/S Norske Shell). UAF, Upper Amundsen Formation; LAF, Lower Amundsen Formation; RP1, Rift Phase 1; PR1, Post-Rift 1; TD, build-up and deflation of the Central North Sea Dome; RP2, Rift Phase 2; PR2, Post-Rift 2.

(Lindsay *et al.* 1993; Yielding *et al.* 1997; Freeman *et al.* 1998). In addition, we estimate the gross rock volume (GRV) of small-scale structural traps present within our projected updip migration route of CO_2 and provide a qualitative categorization of our confidence in the across-fault seal potential. Our results provide insights into the structural evolution of faults within the Aurora storage site and fault

control over CO_2 storage. Consequently, our work builds confidence that faults positively influence CO_2 trapping and plume migration at Aurora.

Geological setting

The Aurora CO_2 storage site is located in the northern part of the Horda Platform, which is a north–south-trending, 300 km-long and 100 km-wide structural high just offshore western Norway (Fig. 1a) (Glennie 1990; Ziegler 1990). The eastern extent of the structural high is defined by the Øygarden Fault Complex (Fig. 1b), which represents a major change in crustal thickness from onshore to offshore (e.g. Færseth *et al.* 1995), whereas the western extent is delimited by the Oseberg fault block and the Viking Graben (e.g. Badley *et al.* 1988; Ziegler 1990; Odinsen *et al.* 2000*a*), the southern extent by the southern Stord Basin (Jarsve *et al.* 2014; Fazlikhani *et al.* 2021), and the northern extent by the Uer and Lomre terraces (Fig. 1b) (e.g. Zhong and Escalona 2020; Tillmans *et al.* 2021).

The crystalline basement beneath the Horda Platform is heterogeneous, comprising Caledonian nappes (e.g. Ziegler 1975, 1982; Gee *et al.* 2008; Corfu *et al.* 2014) and, in some locations, overlain by Devonian low-grade metasediments (Osmundsen *et al.* 2000; Osmundsen and Andersen 2001; Sturt and Braathen 2001). The structural architecture of the basement formed due to contractional tectonics during the Caledonian Orogeny (460–400 Ma) (e.g. Coward *et al.* 2003; Gee *et al.* 2008; Corfu *et al.* 2014), followed by Late Devonian gravitational collapse (e.g. Norton *et al.* 1986; Andersen and Jamtveit 1990; Braathen *et al.* 2000, 2018*b*; Osmundsen and Andersen 2001; Sturt and Braathen 2001; Osmundsen *et al.* 2006; Fossen 2010). Furthermore, some advocate that renewed contraction occurred during the Variscan Orogeny (400–300 Ma) (Ziegler 1975; Coward 1990), while others promote crustal-scale corrugations associated with major extensional detachments and metamorphic core complexes (Wiest *et al.* 2020).The latter is well expressed in the onshore domains in Norway (Braathen and Erambert 2014; Wiest *et al.* 2021).

The first major rift phase that resulted in the current-day structural expression within the Horda Platform occurred during the Late Permian–Early Triassic (e.g. Glennie 1990; Steel and Ryseth 1990; Ziegler 1990; Færseth *et al.* 1995; Fazlikhani *et al.* 2017; Phillips *et al.* 2019; Mulrooney *et al.* 2020). East–west extension led to the formation of large, basement-involved and predominately north–south-striking faults with throws of up to 5 km on the Horda Platform (i.e. first-order faults: Steel and Ryseth 1990; Færseth 1996; Fazlikhani *et al.* 2017). This includes the Øygarden Fault Complex, and the Vette, Tusse, Svartalv and Troll fault zones (Fig. 1b). Locally, these faults deviate from the north–south trend and align approximately with NW–SE- or NE–SW-orientated Caledonian and Devonian structural grains (Færseth *et al.* 1995; Whipp *et al.* 2014). During Rift Phase 1, large north–south-orientated sub-basins formed, which were filled with up to 3 km-thick synrift siliciclastic wedges mainly comprising the Early–Late Triassic Hegre Group (Fig. 2) (Steel and Ryseth 1990; Ravnås *et al.* 2000; Lervik 2006; Jarsve *et al.* 2014; Phillips *et al.* 2019; Würtzen *et al.* 2021).

Rift Phase 1 was followed by a period dominated by relative tectonic quiescence and thermal subsidence from the Middle Triassic to the Early Jurassic (i.e. the inter-rift period: Roberts *et al.* 1993; Steel 1993; Færseth 1996). During this inter-rift period, subsidence due to thermal cooling and sedimentary loading formed a broad basin in the northern North Sea, which was filled with clastic sediments sourced from the Norwegian and Scottish highlands such as the continental and fluvial-deltaic to shallow-marine sediments of the Statfjord, Dunlin and Brent groups (Fig. 2) (Deegan and Scull 1977; Helland-Hansen *et al.* 1992; Marjanac and Steel 1997). In the Horda Platform, the geometry of these stratigraphic intervals is relatively tabular and exhibit a minor influence from faulting (e.g. Bartholomew *et al.* 1993; Steel 1993; Nottvedt *et al.* 1995; Bell *et al.* 2014; Whipp *et al.* 2014).

Renewed rifting took place during the Middle Jurassic–Early Cretaceous (i.e. Rift Phase 2: Badley *et al.* 1988; Underhill and Partington 1993; Cowie et al. 2005; Bell *et al.* 2014; Duffy *et al.* 2015; Phillips *et al.* 2019; Mulrooney *et al.* 2020). The initiation of Rift Phase 2 occurred in the Middle–Late Jurassic after the collapse of the Central North Sea Dome (Underhill and Partington 1993; Roberts *et al.* 1995; Færseth 1996; Odinsen *et al.* 2000*a*; Davies *et al.* 2001; Coward *et al.* 2003). In the Horda Platform, Permian–Triassic first-order faults were reactivated during rifting, which also led to the formation of smaller, predominately north–south- to NW–SE-striking faults with displacements of <100 m (i.e. second-order faults: Færseth *et al.* 1995; Færseth 1996; Bell *et al.* 2014; Whipp *et al.* 2014; Duffy *et al.* 2015; Deng *et al.* 2017; Mulrooney *et al.* 2020). Compared to Rift Phase 1, deformation was less intense (Odinsen *et al.* 2000*a*, *b*) and diachronous with strain localization in the Viking Graben (Bell *et al.* 2014; Phillips *et al.* 2019). Rift Phase 2 synrift sediments are represented by the fully marine Viking Group, which comprises Late Jurassic siliciclastic wedges in the northern North Sea (Vollset and Doré 1984; Sneider *et al.* 1995; Stewart *et al.* 1995; Husmo *et al.* 2002) that interfinger basinwards with shelfal deposits (Steel 1993; Nottvedt *et al.* 1995; Dreyer *et al.* 2005) and is overlain by deep-marine, organic-rich mudstones (Fig. 2) (Vollset and Doré 1984).

While rifting generally ceased during the Early Cretaceous (e.g. Færseth 1996; Gabrielsen *et al.* 2001; Coward *et al.* 2003; Bell *et al.* 2014; Phillips *et al.* 2019), thermal cooling and sedimentary loading led to the continued accumulation of displacement along some of the first-order faults (Bell *et al.* 2014; Whipp *et al.* 2014; Phillips *et al.* 2019; Mulrooney *et al.* 2020). A widespread unconformity formed in the North Sea, the northern North Sea Unconformity Complex (NNSUC: Gabrielsen *et al.* 2001; Kyrkjebø *et al.* 2004), which generally represents the transition from synrift and post-rift (Badley *et al.* 1988; Nottvedt *et al.* 1995; Gabrielsen *et al.* 2001; Kyrkjebø *et al.* 2004). The NNSUC is overlain by deep-water siliciclastic and carbonate successions of the Cromer Knoll and Shetland groups as a result of subsidence and sea-level rise during the Cretaceous (Fig. 2) (Deegan and Scull 1977; Brekke *et al.* 2001). Silty claystones of the Rogaland and Hordaland groups were deposited during the Paleogene and Neogene in a thermally subsiding basin (Fig. 2) (Gabrielsen *et al.* 2001; Faleide *et al.* 2002; Anell *et al.* 2012). The Upper Cretaceous–Middle Miocene successions in the Horda Platform are intersected by a polygonal fault system formed during the Eocene–Early Oligocene (Fig. 3) (Clausen *et al.* 1999; Eidvin and Rundberg 2007; Eidvin *et al.* 2014; Mulrooney *et al.* 2020).

Data and methodology

To perform structural characterization and assessment of across-fault seal presence within the Aurora storage site, we interpreted the storage complex and displacing faults. In the following sections, the data base, interpretations, and theoretical concepts applied in our study are presented.

Seismic data and well control

We utilized the 3D seismic dataset GN10M1 to interpret geological features and create a structural geomodel (Fig. 1b). The survey was acquired from Gassnova, and represents a pre-stack merge of three 3D surveys (GN1001, NPD-TW-08-4D-TROLLCO2 and NH0301) imaged with SEG normal polarity, a zero-phase wavelet, and inline and cross-line spacing of 25 and 12.5 m, respectively. The GN10M1 3D seismic survey covers *c.* 1370 km^2 in the

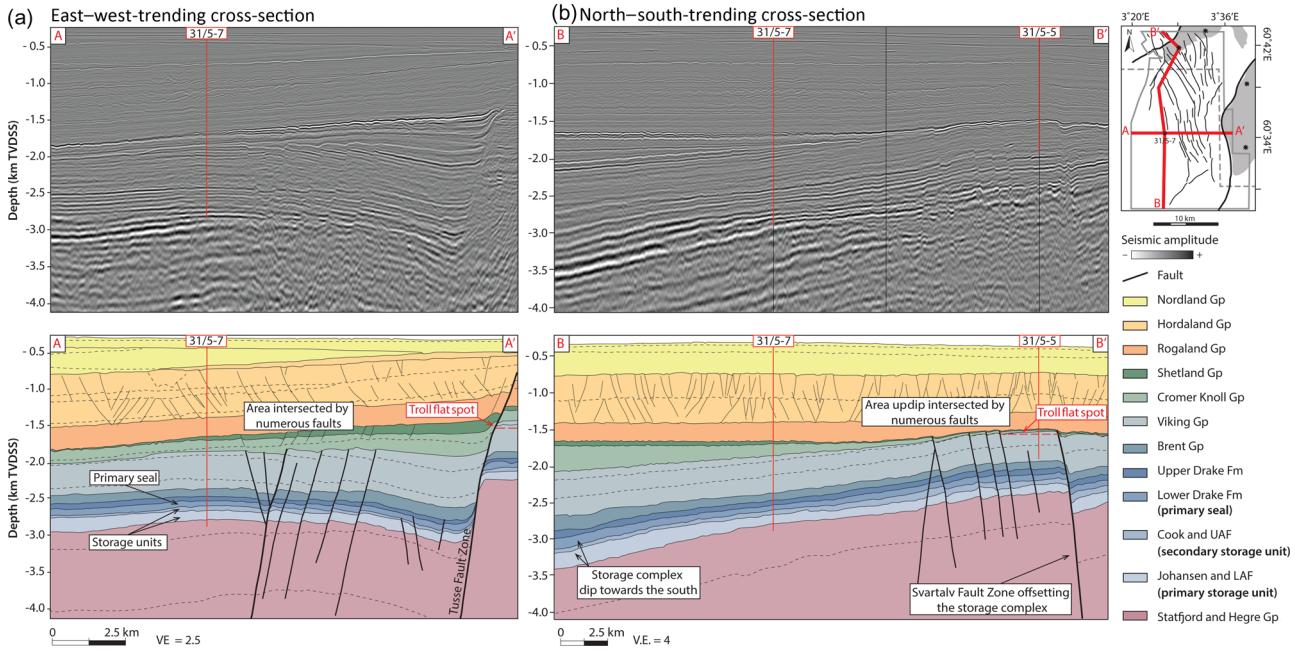

Fig. 3. Depth-converted seismic sections running (**a**) west to east (A–A′) and (**b**) south to north (B–B′) through our study area in the GN10M1 merged survey. Both sections intersect the location of well 31/5-7. The upper parts of each figure show the uninterpreted seismic, whereas the bottom parts show the corresponding interpreted sections with stratigraphic units and faults. The inset map shows the location of the seismic sections in our study area. The Troll hydrocarbon accumulation is highlighted with a red dashed line in the figures. UAF, Upper Amundsen Formation; LAF, Lower Amundsen Formation; VE, vertical exaggeration.

Norwegian quadrants 31/2, 31/5 and the northernmost part of 31/8 within the Horda Platform, which comprises the Troll West Field and the northern parts of the exploitation licence EL001 (Fig. 1b). As a result, the lateral extent of most structural features in the proximity to well 31/5-7 is covered by GN10M1. The maximum depth record of the survey is 4000 ms TWT (two-way travel time), imaging predominately Mesozoic–Cenozoic successions and faults that deform them, including those that displace the Lower Jurassic storage complex. 2D seismic surveys were used to interpret deeper structures and assess basement-involvement of faults. We delimited our structural geomodel to a smaller area (420 km^2) within the GN10M1 survey to focus specifically on faults and the storage complex within the projected updip migration path and in proximity to well 31/5-7 (Fig. 1b). This also enables a comparison between previous structural characterization studies (e.g. Whipp *et al.* 2014; Duffy *et al.* 2015) and across-fault seals (e.g. Bretan *et al.* 2011; Bretan 2017; Osmond *et al.* 2022) in the Troll West Field. The velocity model constructed by Michie *et al.* (2021) was used herein for depth conversion of the time-migrated GN10M1 data, 2D seismic lines and seismic interpretations. This ensures a more accurate portrayal of fault and horizon geometries, and, thus, improves the validity of the fault seal (Lyon *et al.* 2004, 2005; Michie *et al.* 2021). Depth conversion also enables derivation of seismic well ties, well-log-based calculations and volumetric estimates. We tied the seismic data to wellbores located within the Troll West Field (31/2-1, 31/5-2 and 31/2-5) and well 31/5-7 located within the exploitation licence EL001. Most well data (location, well trajectory, formation tops, checkshots and well-log curves) were acquired from the Norwegian Petroleum Directorate (NPD) and the DISKOS data repository, whereas data from well 31/5-7 were made publicly available by the Northern Lights JV DA (Equinor ASA 2022).

Seismic interpretation and modelling

To create a detailed geomodel of the envisaged storage complex in Aurora, we interpreted six horizons using Petrel E&P software. This includes the top Statfjord Group, top Johansen Formation, top Cook Formation, top Lower Drake Formation, top Upper Drake Formation and top Brent Group (Fig. 2). We were unable to interpret either the top Upper or top Lower Amundsen Formation horizons (UAF and LAF in Fig. 2). This is because both intervals lie close to or below the vertical seismic resolution at the depth in which they reside within well 31/5-7 (7 and 14 m, respectively) and because they are not considered regional seals (Gassnova 2012; Sundal *et al.* 2015). Each horizon was interpreted at least every 10th inline and cross-line, creating a 120 × 250 m interpretation grid. In areas with higher structural complexity or proximity to faults of interest, a denser spacing interval was applied. The horizon interpretation grid was then autotracked to create a continuous gridded surface, which we then used to generate variance maps and thickness maps, and to calculate gross rock volumes (GRVs) of structural traps. For simplicity, we define structural traps as any geometrical volume within the intended storage units bound by faults and top seals that could create separate CO_2 accumulations. Subsequently, we subdivided the storage units into a primary storage unit comprising the Lower Amundsen and Johansen formations, and a secondary storage unit comprising the Upper Amundsen and Cook formations (Figs 2 and 3). Similar to Gassnova (2012) and Thompson *et al.* (2022), we subdivided the Drake Formation into two units, where the Lower Drake Formation is more mud-rich and is envisaged to be the primary seal for injected CO_2, and the Upper Drake Formation is characterized by mixed shales, silts and, potentially, sandstone lenses with less seal potential (Figs 2 and 3). Units that are not part of the intended storage complex within the Aurora storage site are referred to as underlying units (i.e. the Statfjord Group) and overlying units (i.e. the Upper Drake Formation and the Brent Group).

We performed detailed interpretations of all seismic-scale faults that displace the storage complex. All faults were interpreted manually with a line spacing of between two and five lines (50–125 m), close to the optimum spacing of 100 m proposed by Cunningham *et al.* (2020) and Michie *et al.* (2021). Fault tips were interpreted with a smaller spacing of one or two lines to map the

resolvable extent. We applied seismic variance attribute analysis (Randen and Sønneland 2005) to highlight and guide our fault interpretation with both horizontal and vertical slices of the seismic volume. All interpreted faults and horizons were then transferred to the Move software suite (PETEX) to create horizon–fault cutoff lines. We applied a similar methodology to Mulrooney *et al.* (2020) when creating the cutoff lines, where cutoff lines are first mapped manually along the horizon and fault intersection, and then projected horizontally onto the fault plane. This ensures high-quality results, reducing the influence of seismic artefacts and erroneous structural orientations near the fault surface. In addition, we used the autotracked interpretation grid, in combination with the horizon interpretation, to achieve a line spacing of between 25 and 250 m when creating the cutoff lines, as recommended by Michie *et al.* (2021).

Structural characterization

We performed structural characterization to assess the influence of faults on plausible CO_2 migration pathways and the presence of structural traps. The horizon cutoff lines were used to generate throw v. depth plots, throw v. distance plots and throw gradients draped onto the interpreted 3D fault surfaces. Throw v. depth profiles (also known as *T*–*z* profiles) were plotted together with expansion index (EI) to determine the depth of fault nucleation and periods of fault activity (e.g. Thorsen 1963; Cartwright and Mansfield 1998; Tearpock and Bischke 2002; Hongxing and Anderson 2007; Jackson and Rotevatn 2013). For an ideal blind fault, the point of maximum throw typically correlates with the fault nucleation point. Multiple throw maxima typically indicate reactivation or vertical linkage of faults (e.g. Cartwright *et al.* 1998; Hongxing and Anderson 2007). The expansion index (Thorsen 1963) represents the ratio of the hanging-wall thickness of an interpreted succession to the corresponding footwall thickness, which is often plotted together with the throw v. depth plot. A ratio >1 indicates that the fault intersected the surface and created accommodation in the hanging wall (i.e. synkinematic sedimentation). To assess the along-strike throw distribution and assess fault linkage types (i.e. hard- or soft-linkage), we created throw v. distance profiles, and also draped calculated throw values onto the interpreted fault surfaces.

Across-fault seal assessment

We investigated the presence of fault seals at the Aurora storage site by assessing two types of across-fault seals: juxtaposition and membrane seals. These are widely accepted sealing mechanisms in petroleum geology (e.g. Downey 1984, 1994; Watts 1987; Allan 1989; Fristad *et al.* 1997; Yielding *et al.* 1997; Lyon *et al.* 2005; Færseth *et al.* 2007), and are envisaged to similarly influence injected CO_2 migration and trapping (e.g. Bretan *et al.* 2011; Karolytė *et al.* 2020; Mulrooney *et al.* 2020; Wu *et al.* 2021; Osmond *et al.* 2022).

Juxtaposition seals occur when the high-permeability storage unit becomes juxtaposed against a low-permeability sealing unit (Watts 1987; Allan 1989; Knipe 1997). To assess the presence of juxtaposition seals, we applied the modelled cutoff lines and assigned simplified lithologies to each interpreted unit, similar to that described in Osmond *et al.* (2022) (i.e. storage, seal, underlying and overlying units: Fig. 2). We inferred the presence of the Upper Amundsen Formation in each of our diagrams based on the average thickness (22 m) in wells 31/5-7, 31/5-2 and 31/2-5 to discuss its potential influence on across-fault migration. Each juxtaposition was then colour-coded to provide a simple and concise overview of areas with or without juxtaposition seals. Areas where the storage unit are self-juxtaposed or juxtaposed against other higher permeability units represent potential across-fault migration.

Membrane seals occur when the fault rock itself holds sealing potential due to mechanisms such as cataclasis, cementation and clay smearing (e.g. Smith 1966; Watts 1987; Fisher and Knipe 1998, 2001; Fossen *et al.* 2007; Pei *et al.* 2015). These mechanisms reduce the pore throat size, thus increasing the pressure required for fluids to enter the fault rock (i.e. the capillary entry pressure: Knipe 1992; Fisher and Knipe 1998; Fossen *et al.* 2007). Previous studies show that clay smear is the dominant factor that leads to reduced pore throat sizes in the northern North Sea (e.g. Knott 1993; Fisher and Knipe 2001; Sperrevik *et al.* 2002; Yielding 2002). It is challenging, however, to directly determine the pore throat size along any point of a subsurface fault. Therefore, we applied shale gouge ratio (SGR: Yielding *et al.* 1997; Freeman *et al.* 1998) and shale smear factor (SSF: Lindsay *et al.* 1993) algorithms to provide an estimate of the clay content in the fault rock and the continuity of smear, respectively. The SGR algorithm considers the clay content of the units that have slipped past a point along the fault and uses this to estimate the fault-rock composition. To calculate SGR values, we obtained thickness and throw estimates from fault cutoff lines, derived the approximate volumetric clay fraction using gamma-ray logs from three wells (31/5-7, 31/5-2 and 31/2-5), and assigned shale- and sandstone-line cutoff values to each well (Lyon *et al.* 2005). We later applied empirical observations for the North Sea from Yielding (2002), who suggested that the onset of membrane seal occurs for SGR > 0.15–0.2. With increasing SGR values, the maximum column height that can be supported by the fault theoretically increases. For SGR > 0.40, no increase in the strength of the seal has been observed (e.g. Bretan *et al.* 2003; Yielding *et al.* 2010).

The SSF algorithm is simply the ratio of fault throw to the thickness of shale beds (Lindsay *et al.* 1993). Similar to Wu *et al.* (2021), we assigned a cutoff value of 0.5 to the derived volumetric clay fraction. Units with more than 50% shale content are considered beds that can smear. We used SSF < 4 to represent continuous smear, values between 4 and 7 potential discontinuities in the smear, and SSF > 7 for no continuous seal (Lindsay *et al.* 1993). 3D juxtaposition and membrane-seal scenarios were then displayed as triangle diagrams (Knipe 1997) and Allan diagrams (Allan 1989) in order to illustrate the influence of each well on the calculated SGR and SSF values. An important consideration is that the SSF algorithm only provides a single value that does not vary vertically along the fault plane and only considers the smearing potential of shale beds, while the SGR includes the clay content for a wider range. Therefore, and to enable comparison against previous studies (Bretan *et al.* 2011; Bretan 2017; Osmond *et al.* 2022), the 3D membrane seal diagrams herein were populated with SGR values.

Structural character

Assessment of the structural character of the storage complex and displacing faults provide evidence for structural evolution and fault linkage within the Aurora storage site. In the following subsections, we present observations and interpretations of the storage complex, fault populations, and detailed measurements of throw, length and expansion indices.

Storage complex

According to the depth-converted seismic data, the storage complex is observed between 2.4 and 2.8 km below mean sea level at the location of well 31/5-7, and exhibits relatively few thickness variations compared to the deeper Triassic and shallower Upper Jurassic–Cretaceous units (Fig. 3). The geometry of the storage complex is in the form of a gentle anticline from east to west and is displaced by numerous normal faults, the nearest of which is just 1.9 km east of well 31/5-7 (Fig. 3a). The anticline has a wavelength

and amplitude of *c.* 14 km and 180 m, respectively. The storage complex is gently dipping towards the south (*c.* 2°: Fig. 3b). Northwards, the storage complex is intersected and displaced by numerous faults with low throw maxima but also by the Svartalv Fault Zone, which offsets the storage complex against the Middle–Upper Jurassic Brent and Viking groups on the hanging-wall side. In map view, the top primary storage unit, secondary storage unit and the primary seal display relatively similar structures (Fig. 4a). That is, deepening towards the SW and SE in the hanging wall of the Tusse Fault Zone (−3.2 to −3.0 km true vertical depth subsea (TVDSS)), and shallowing towards the north (−2.2 to −2 km TVDSS) in the footwall of the Svartalv Fault Zone and towards the Troll licence.

While the thickness of the storage complex is relatively tabular compared to Triassic and Upper Jurassic–Cretaceous synrift units, some thickness variations are apparent (Fig. 4b). The primary storage unit measures, on average, 140 m in thickness and displays thickening towards the SW to *c.* 260 m. Some thinning of the primary storage unit is observed just east of well 31/5-7 to *c.* 110 m. The secondary storage unit is significantly thinner than the primary storage unit and measures, on average, 35 m, showing signs of thickening north of well 31/5-7 to *c.* 100 m. The overlying primary seal shows an overall tabular thickness of 80–90 m, with an average of *c.* 85 m.

Fault populations

The Lower Jurassic storage complex within the Aurora storage site is displaced by numerous faults, as observed from the variance attribute map of the top secondary storage unit (Fig. 5a). We

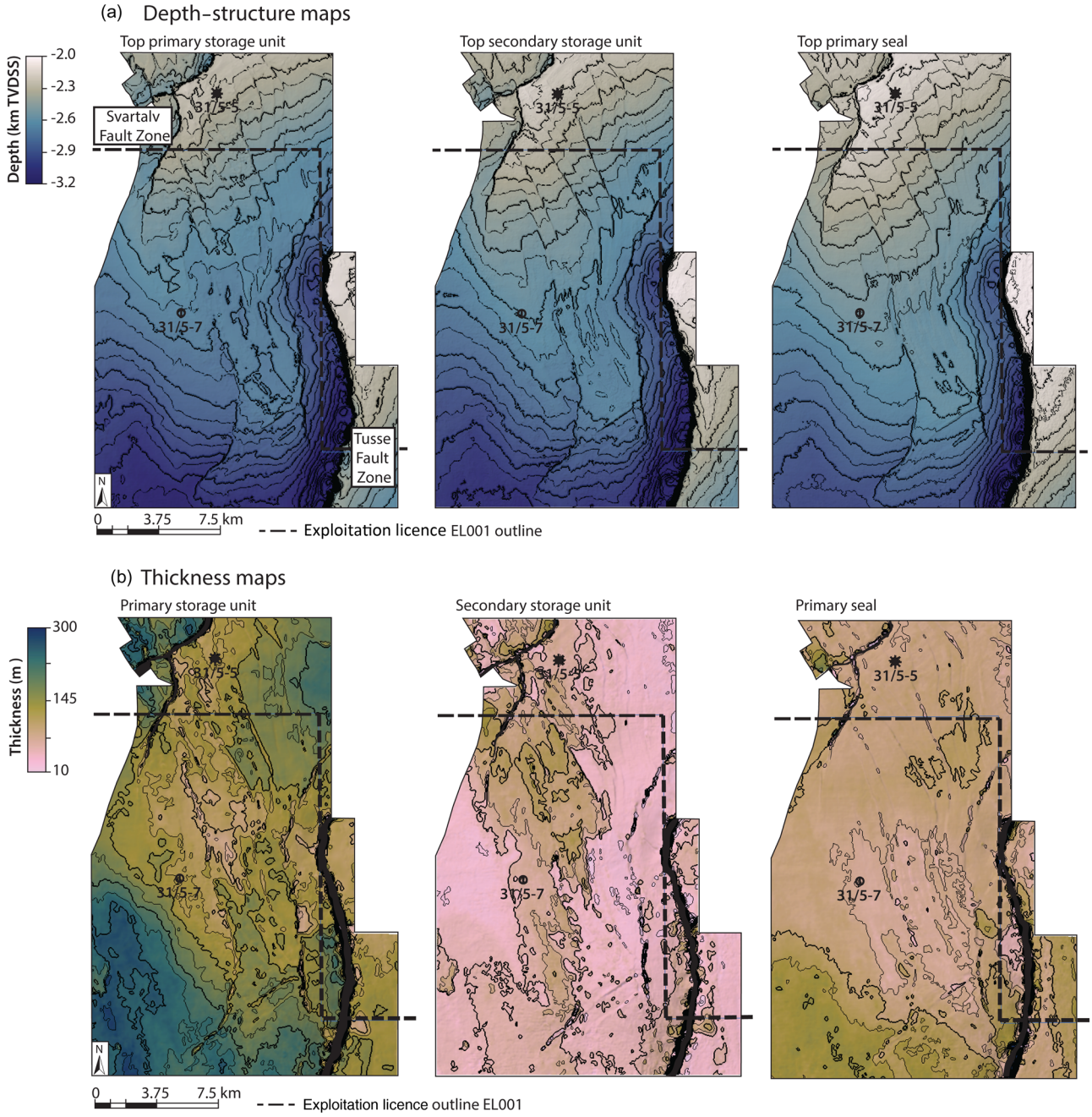

Fig. 4. (**a**) Depth structure maps of the top primary storage, top secondary storage and top primary seal units are displayed with a contour interval spacing of 50 m (bolded every 100 m starting at −2000 m TVDSS). (**b**) Thickness maps of the primary storage, secondary storage and primary seal units are displayed with a contour interval spacing of 25 m (bolded every 50 m starting at 10 m). The location of the Svartalv and Tusse fault zones are annotated in the depth structure map of the primary storage unit, and the EL001 exploitation licence boundary is indicated with a black dashed line. Scientific colour bars (version 7.0.0) are sourced from Crameri (2021).

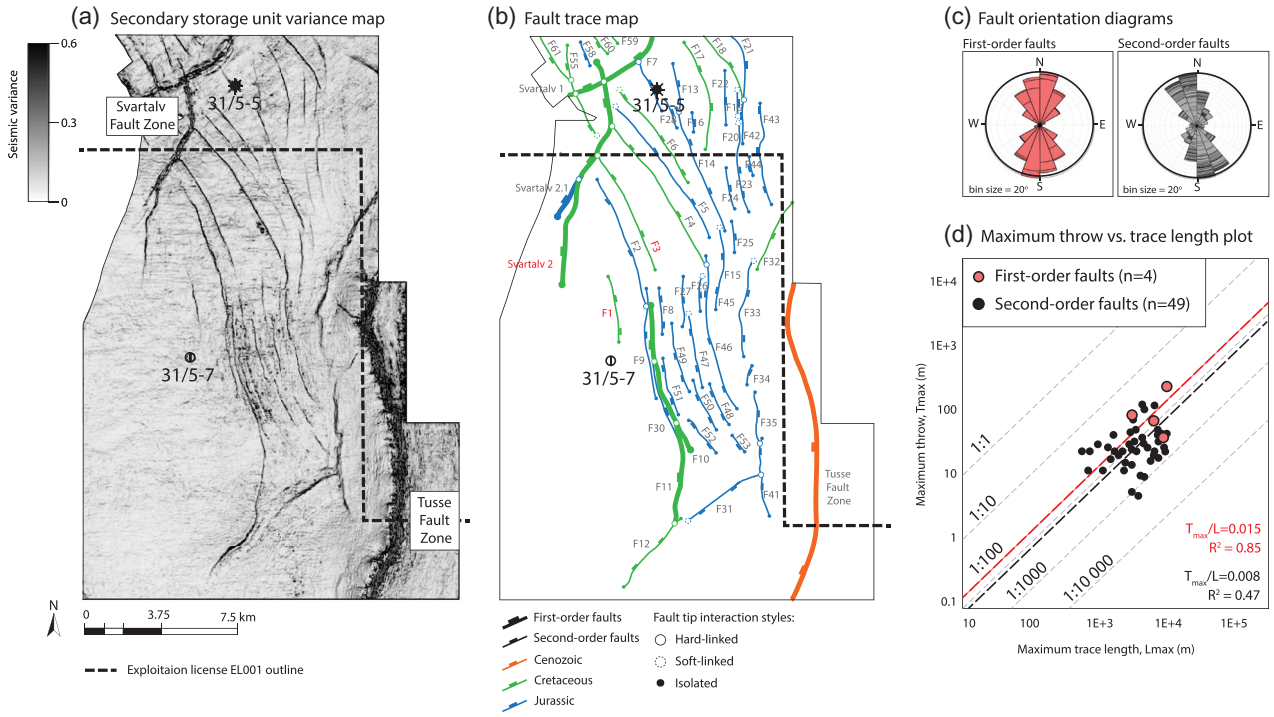

Fig. 5. (**a**) Variance map created by extracting attributes from the interpreted depth–structure map of the top secondary storage unit. (**b**) Fault-trace map showing the lateral extent of interpreted faults at the depth of the top secondary storage unit. The upsection and downsection extent of the interpreted faults are indicated using colour coding and the thickness of fault traces, respectively. Key faults used in throw and across-fault seal assessment herein are labelled in red. The nature of the fault interaction is indicated as hard-linkage, soft-linkage and isolated fault tips. (**c**) Orientation of first- and second-order faults have been sorted into bins of 20° and plotted in terms of the frequency of a particular orientation. (**d**) Maximum throw v. length plot for the first- and second-order faults with associated trend lines and equations. Faults that are only partly imaged within our study area have not been included to reduce sampling bias. Measurements are taken from the top secondary storage depth–structure map and are summarized in Appendix A.

interpreted 69 faults in total within our study area (Fig. 5b), and a complete list of fault attributes is shown in Appendix A. Overall, our measurements of fault orientations, throw maxima and trace lengths conform to trends observed within the Troll West and East fields (Whipp *et al.* 2014) (Fig. 5c, d). Similar to Gabrielsen (1984), we subdivided the interpreted faults into separate populations based on whether they displace the basement (i.e. whether there is basement involvement). These are: (i) first-order faults that extend down from the storage complex level and displace the basement–cover contact; and (ii) second-order faults that are largely restricted to the sedimentary units and have no basement involvement.

First-order faults

Six faults within our study area are categorized as first-order faults, displacing the basement–cover contact by 0.5–3 km (measured from depth-converted 2D seismic lines: Fig. 5b). The vertical extent of first-order faults is shown in Appendix B. This includes segments of the Svartalv (i.e. Svartalv 1, Svartalv 2 and Svartalv 2.1) and Tusse fault zones, as well as two north–south-striking faults located just east of well 31/5-7 (i.e. F10 and F11: Fig. 5b). Upsection, most first-order faults tip out within the Cretaceous stratigraphy or the NNSUC (Gabrielsen *et al.* 2001; Kyrkjebø *et al.* 2004). However, the Tusse Fault Zone displaces shallower Cenozoic units. Measured from the top Cook Formation (i.e. top secondary storage unit), the mean orientation of the first-order faults is north–south (182°: Fig. 5c) within the study area. Furthermore, their average trace length is *c.* 7 km, and their throw maxima ranges from 43 to 940 m, with the Tusse Fault Zone exhibiting the greatest throw. In section view, the first-order faults show changes in dip angle from *c.* 60° in the Jurassic units to 30° in the crystalline basement (i.e. a listric geometry: Appendix B). While most first-order faults exhibit isolated fault tips, some show hard-linkage (e.g. Svartalv 1 and Svartalv 2).

Second-order faults

Sixty-three faults mapped in our study area are categorized as second-order faults as they exhibit no apparent basement involvement (Fig. 5b). In contrast to the first-order faults, the second-order faults show no preferential dip direction, and are relatively planar and steeply dipping (55°–60°) in cross-section (Appendix B). The mean orientation of the second-order faults is north–south (171°: Fig. 5c), which is slightly anticlockwise to the first-order faults. However, both the strike and fault-trace geometry change within our study area. Just east of well 31/5-7, the strike of the second-order faults is predominately north–south and their traces are concave towards the hanging wall of the Tusse Fault Zone. Towards the north, their overall strike changes to NW–SE or NNW–SSE, and their traces are concave towards the SW and the footwall of the Svartalv Fault Zone (Fig. 5a, b). Our interpretations indicate that vertical extents are significantly shorter for second-order faults compared to those of first-order faults. Downsection, the second-order faults tip out within the Upper Triassic–Jurassic strata, while upsection they terminate within the Jurassic and Cretaceous strata or towards the NNSUC (Fig. 5b). On average, second-order fault-trace lengths are *c.* 3.6 km long, and the majority of the faults have throw maxima between 15 and 50 m measured from the top Cook Formation. In contrast to the first-order faults, the second-order fault measurements plot with almost half the maximum throw v. length ratio (T_{max}: Fig. 5d). Most second-order faults within our study area exhibit isolated fault tips. However, several NW–SE-striking second-order faults in the northern part of the study area are hard- or soft-linked with the first-order Svartalv 1 and Svartalv 2, potentially creating either structural traps or relay ramps that may facilitate fluid migration.

Throw, length and expansion index

Detailed 3D fault throw diagrams, throw v. length profiles, throw v. depth profiles and expansion index profiles are presented for three

key faults (Svartalv 2, F1 and F3: Figs 5b and 6–8) located within the updip projected migration pathway for CO_2 (i.e. northwards from well 31/5-7). An overall north–south-striking (188°) segment of the Svartalv Fault Zone (herein called Svartalv 2: Fig. 5b) extends into the northwestern parts of our study area and tips out *c.* 4.6 km NE of well 31/5-7. Svartalv 2 potentially represents the western border for CO_2 migration; thus, the along-strike throw distribution at the depth of the storage complex is of interest. Svartalv 2 is *c.* 11 km long and the throw contours indicate an asymmetrical pattern, with a relatively flat upper tip line (Fig. 6a). All interpreted horizon surfaces exhibit relatively similar throw v. length profiles (Fig. 6b), with the throw maximum (*c.* 300 m) coinciding with the intersection point of the NW–SE-striking second-order F3 fault in the footwall of Svartalv 2. A similar local throw maximum (270 m) is located at the intersection of F4 and Svartalv 2. A more dramatic decrease in throw (100–150 m) is present where the first-order Svartalv 1 and Svartalv 2.1 faults are hard-linked with Svartalv 2. As seen in both the throw v. length profile (Fig. 6b) and the throw v. depth profile (Fig. 6c), Svartalv 2 exhibits increasing throw downsection, with an absolute maximum throw of 550 m located at the basement–cover contact (not

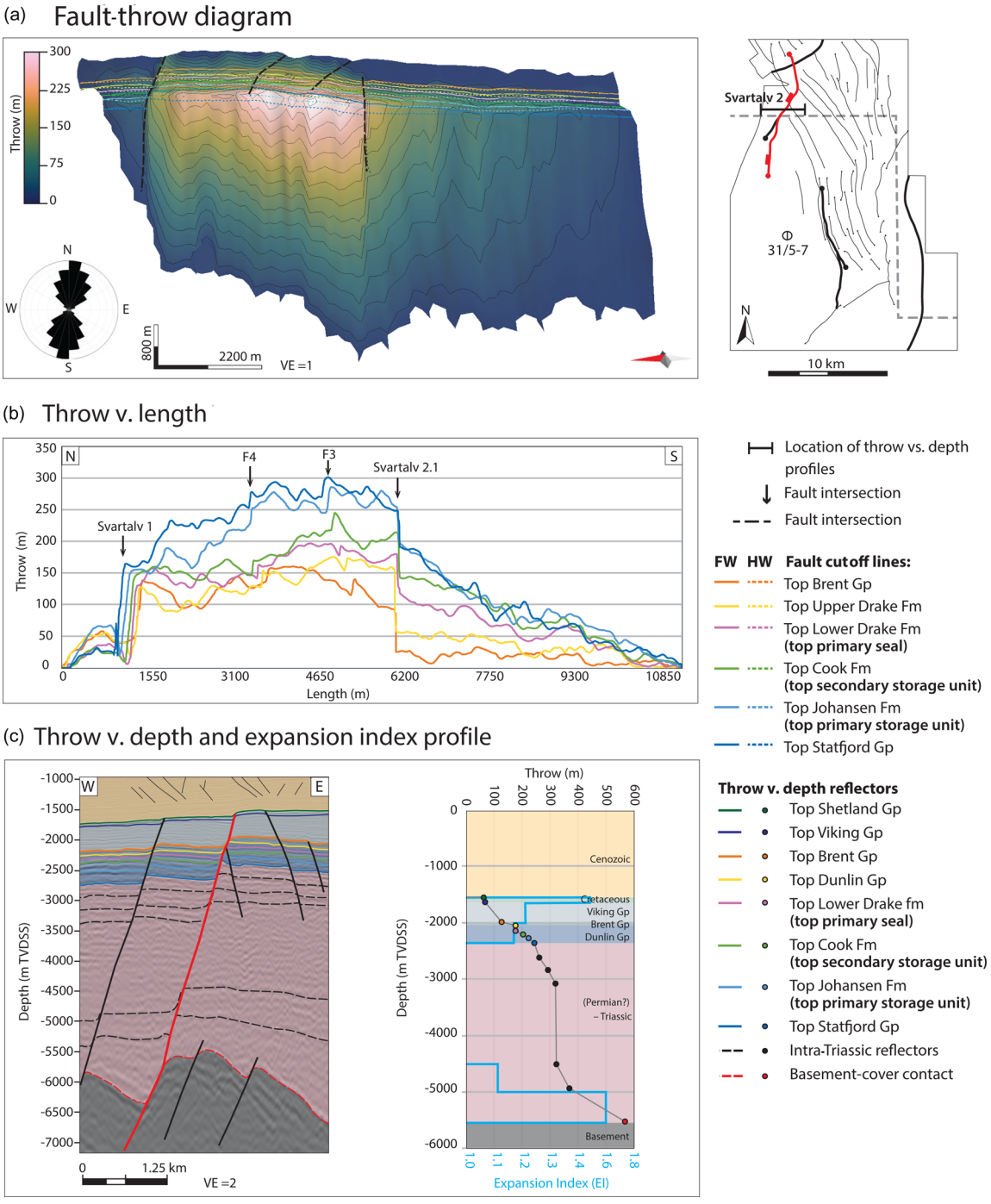

Fig. 6. Throw assessment figures for the first-order Svartalv 2 fault. (**a**) Three-dimensional fault-throw diagram of Svartalv 2 viewed from the hanging-wall side and showing horizon–fault intersection (cutoff) lines. Contour spacing is 20 m. A fault-orientation diagram is displayed with a bin size of 15°. Note that throw values below the Statfjord Group hanging-wall cutoff line have been extrapolated and are not likely to be representative. (**b**) Throw v. length profile for Svartalv 2 showing the lateral variations in throw for the Lower–Middle Jurassic horizons. Fault-intersection locations are indicated in the profiles. See Figure 5b for an overview of fault names. (**c**) Throw v. depth and expansion index profile for Svartalv 2 (red line) showing the vertical variations in throw and hanging-wall expansion, respectively. Interpreted seismic sections (left) show the locations of throw and thickness measurements. Scientific colour bar (version 7.0.0) in (a) is sourced from Crameri (2021).

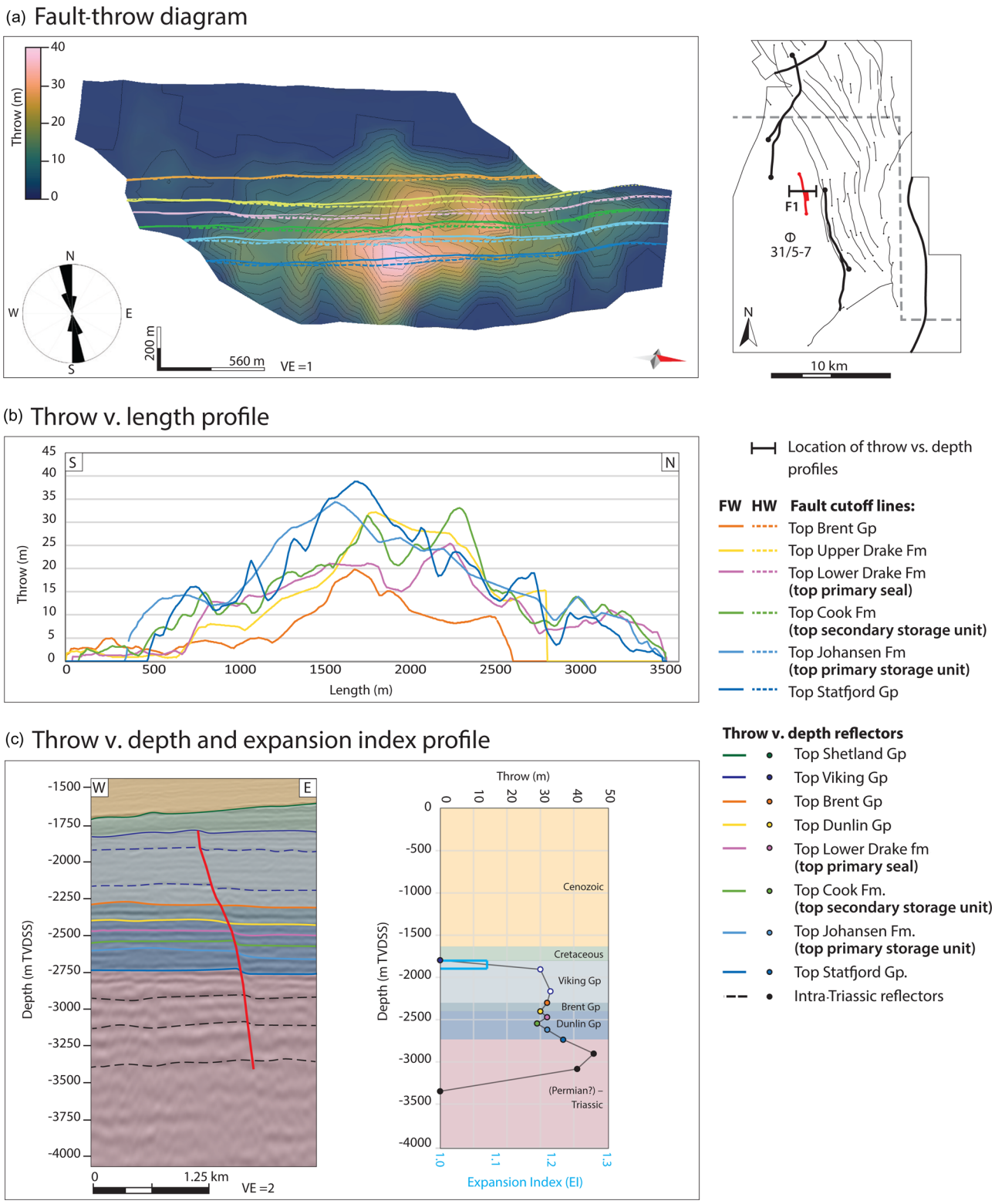

Fig. 7. Throw-assessment figures for the second-order F1 fault. (**a**) Three-dimensional fault-throw diagram of F1 viewed from the hanging-wall side and showing the horizon–fault intersection (cutoff) lines. Contour spacing is 2 m. A fault-orientation diagram is displayed with a bin size of 15°. Note that throw values below the Statfjord Group hanging-wall cutoff line have been extrapolated and are not likely to be representative. (**b**) Throw v. length profile for F1 showing the lateral variations in throw for the Lower–Middle Jurassic horizons. (**c**) Throw v. depth and expansion index profile for F1 (red line) show the vertical variations in throw and hanging-wall expansion, respectively. Interpreted seismic sections (left) show the locations of throw and thickness measurements. Scientific colour bar (version 7.0.0) in (a) is sourced from Crameri (2021).

modelled in Fig. 6a). Clear wedge-shaped geometries are present in the Permian(?)–Early Triassic units, resulting in expansion indices of 1.1–1.6. Expansion indices >1 are also present for Jurassic–Cretaceous units (EI between 1.17 and 1.2); however, wedge-shaped geometries are less apparent (Fig. 6c).

The F1 fault represents a north–south-striking (352°) isolated second-order fault located just 700 m NE (i.e. updip) of well 31/5-7 (Figs 5b and 7a). Compared to Svartalv 2, F1 is significantly shorter, with a maximum trace length of 3.5 km measured along the top Cook Formation surface. The throw v. length profile shows a

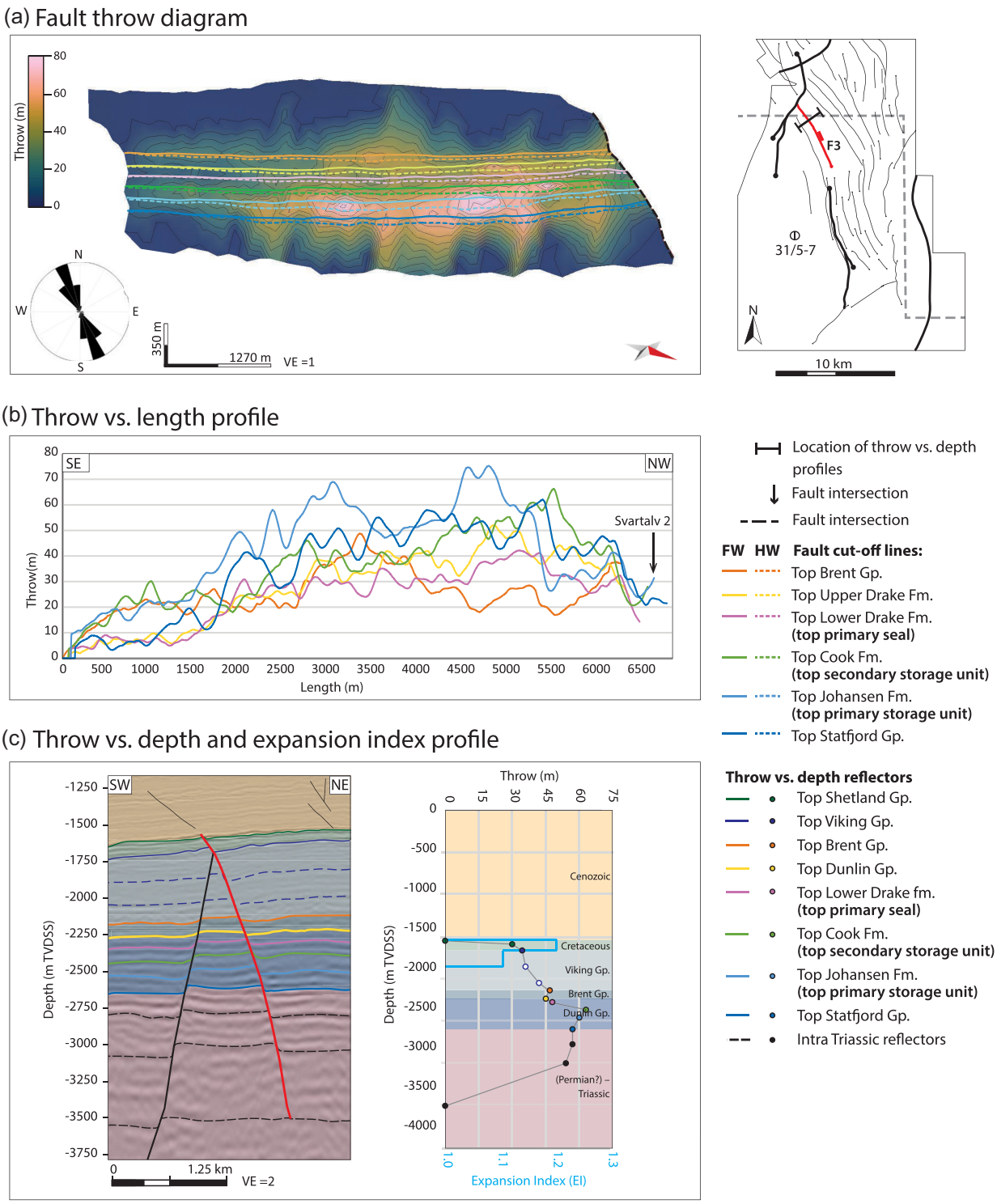

Fig. 8. Throw-assessment figures for the second-order F3 fault. (**a**) Three-dimensional fault-throw diagram of F3 viewed from the hanging-wall side and showing horizon–fault intersection (cutoff) lines. The contour spacing is 5 m. The fault-orientation diagram is displayed with a bin size of 15°. Note that throw values below the Statfjord Group hanging-wall cutoff line have been extrapolated and are not likely to be representative. (**b**) Throw v. length profile for F3 showing the lateral variations in throw for the Lower–Middle Jurassic horizons. Fault-interaction locations are indicated in the profiles. See Figure 5b for an overview of fault names. (**c**) Throw v. depth and expansion index profile for F3 (red line) show the vertical variations in throw and hanging-wall expansion, respectively. Interpreted seismic sections (left) show the locations of throw and thickness measurements. Scientific colour bar (version 7.0.0) in (a) is sourced from Crameri (2021).

local maximum throw of 40 m measured at the top Statfjord Formation and decreasing throw upsection (Fig. 7b). The throw of F1 decreases to zero towards the northern and southern fault tip, as well as upsection and downsection (Fig. 7b, c). In cross-section (Fig. 7c), the throw maximum (48 m) of F1 is located within the Triassic units and a second smaller-order throw maximum (32 m) within the Upper Jurassic Viking Group. Some hanging-wall expansion is observed in the Upper Jurassic succession; again, however, wedge-shaped geometries are not easily distinguishable in the seismic data (Fig. 7c).

The F3 fault is a NNW–SSE-orientated (336°) second-order fault that intersects Svartalv 2 on its footwall side, and is representative of the multiple NW–SE-orientated second-order faults located updip from well 31/5-7 within our study area (e.g. F2, F4, F5 and F6:

Fig. 5b). Measured from the top Cook Formation, F3 is 6.8 km long, displaying an overall elliptical shape and a slightly flatter upper tip line compared to the one at its base (Fig. 8a). From the throw v. length profile, maximum throw values of *c.* 70–75 m are spread out over a wider area, compared to F1, which is located NW off-centre (Fig. 8b). Towards the southeastern fault tip, the throw decreases to zero, while the throw gradient is steeper at the northwestern tip. Along the intersection with Svartalv 2, the F3 fault has throws ranging from 10 to 30 m within the interval of the interpreted horizons. Similar to Svartalv 2 and F1, F3 exhibits decreasing throw upsection (Fig. 8b). F3 also displays a similar throw v. depth and expansion index profile to F1, where throw decreases to zero both upsection and downsection, and expansion index exceeds 1 for Upper Jurassic and Cretaceous units (Fig. 8c). In contrast to F1, the throw absolute maximum is located slightly shallower within the Lower Jurassic units.

Across-fault seals

The presence of across-fault seals would influence migration pathways of injected CO_2 in the Aurora storage site. In the following subsections, we present results from SGR and SSF triangle diagrams from wells within and in proximity to Aurora. We also show detailed juxtaposition and membrane-seal diagrams, applying the SGR algorithm, for three key faults (Svartalv 2, F1 and F3).

SGR and SSF triangle diagrams

We created 1D triangle diagrams (Knipe 1997) using the gamma-ray log from three wells (31/5-7, 31/5-2 and 31/2-5) and populated them with calculated SGR and SSF values (Fig. 9). To include information from both the hanging-wall and the footwall sides, wells 31/5-7 and 31/5-2 were used to create SGR diagrams for

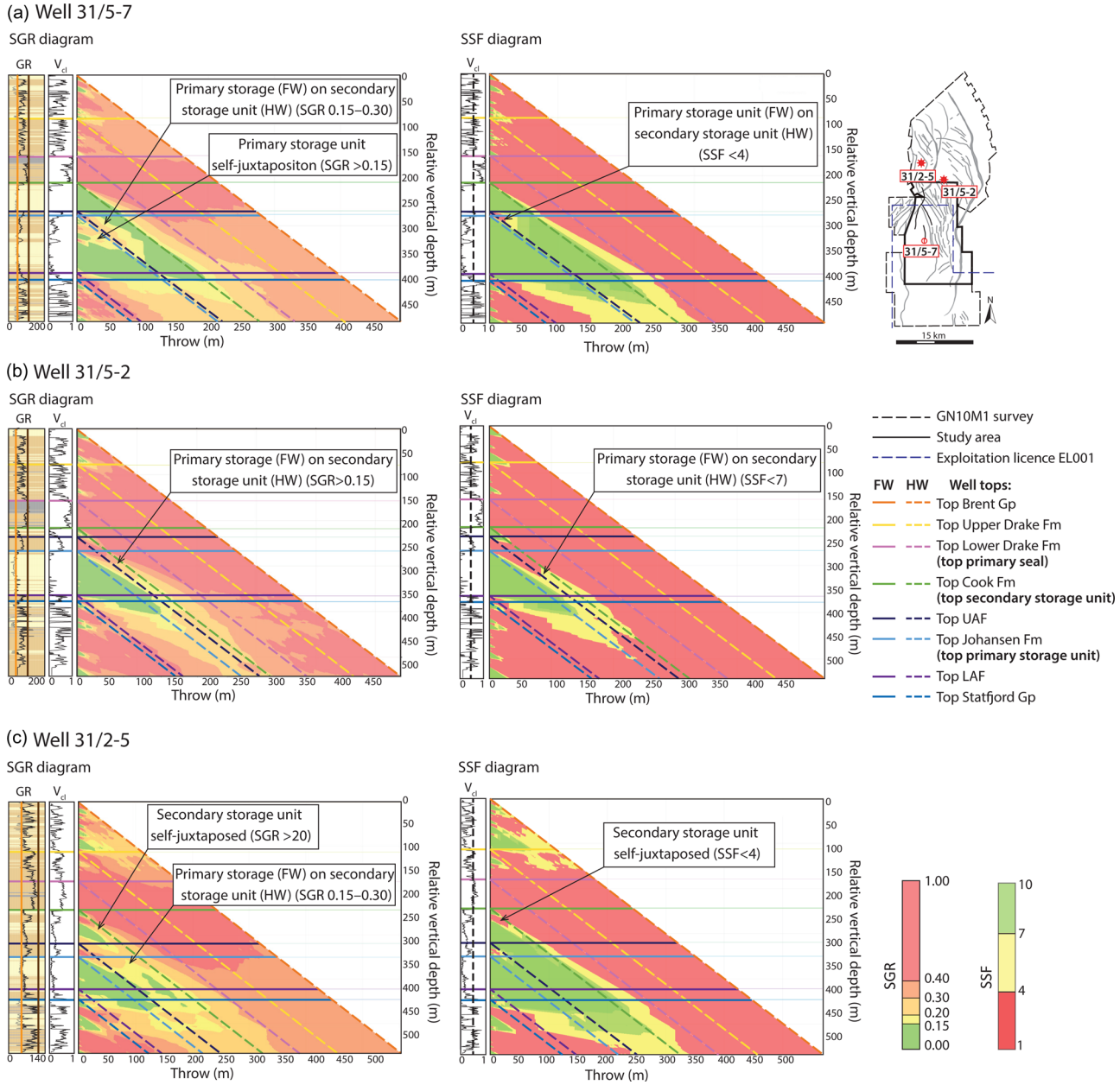

Fig. 9. 1D triangle diagrams populated with shale gouge ratio (SGR) and shale smear factor (SSF) values calculated using the gamma-ray (GR) log from three wells (31/5-7, 31/5-2 and 31/2-5) in the vicinity of the key faults (i.e. Svartalv 2, F1 and F3: Fig. 5b). Wells 31/2-5 and 31/5-7 were used to create the SGR diagram of Svartalv 2, and wells 31/5-2 and 31/5-7 were used for F1 and F3 in Figure 10b. Gamma-ray log and normalized volumetric clay fraction (V_{cl}) are presented to the left of each diagram. The black dashed line in the V_{cl} log represents the 0.5 cutoff value for the SSF diagrams. The following sandstone and shale cutoffs were selected for each well: (**a**) 60 and 130° API, (**b**) 60 and 106° API° and (**c**) 50 and 115° API°. FW, footwall; HW, hanging wall; UAF, Upper Amundsen Formation; LAF, Lower Amundsen Formation.

faults F1 and F3, whereas well 31/5-7 and 31/2-5 were used for Svartalv 2.

Well 31/5-7 is located 0.7 km south of F1, 4.7 km SW of F3 and 4.4 km SE of Svartalv 2. Figure 9a shows that where the primary and the secondary storage units are self-juxtaposed, the calculated SGR is primarily <0.15. An exception is shown where thin clay-rich layers exhibiting higher gamma-ray values (80–90° API) will contribute to higher SGR values (>0.15) where the primary storage unit is self-juxtaposed. Where the primary storage unit in the footwall is juxtaposed against the secondary storage unit in the hanging wall, SGR will primarily be <0.15, whereas SSF will be >7. However, the presence of a thin (7 m) Upper Amundsen Formation contributes to higher SGR values (0.15–0.30) for throws <120 m and lower SSF values (<4) for throws <25 m. In general, calculated SGR exceeds 0.30 and SSF will be <4 where the storage units in the footwall become juxtaposed against overlying units (i.e. the Upper Drake Formation and the Brent Group) in the hanging wall. Well 31/5-2 is located 9.3 km NE of F3 and 13.9 km NE of F1. In contrast to well 31/5-7, well 31/5-2 shows overall higher calculated SGR values partly due to a thicker Upper Amundsen Formation (29 m) and a thinner, less-sandy, Cook Formation (20 m; Fig. 9b). Consequently, higher SGR values (>0.15) and lower SSF values (<7) will occur where the primary storage unit in the footwall is juxtaposed against the secondary storage unit in the hanging wall. Well 31/2-5 is located 7.8 km NW of Svartalv 2 on the hanging-wall side. The triangle diagram in Figure 9c shows relatively similar results to the aforementioned wells. However, higher SGR values (>0.20) and lower SSF values (<4; for throws <40 m) are present where the upper parts of the secondary storage unit are self-juxtaposed in the model. Furthermore, higher SGR values (0.15–0.30) are present where the upper parts of the primary storage unit in the footwall are juxtaposed against the secondary storage unit in the hanging wall. In contrast, SSF > 7 is modelled where the primary storage unit in the footwall is juxtaposed against the secondary storage unit in the hanging wall.

Synthesis of SGR and SSF triangle diagrams derived from three wells show that: (i) the clay-rich Upper Amundsen Formation thickens towards the north, consequently contributing to higher SGR values (0.20–0.40) and lower SSF values (<4) where the upper parts of the primary storage unit in the footwall are juxtaposed against the secondary storage unit in the hanging wall; (ii) heterogeneities within the primary and secondary storage units result in SGR values exceeding 0.15 and SSF values less than 4 at storage unit self-juxtaposition; and (iii) where the storage units in the footwall are juxtaposed against overlying units in the hanging wall, SGR > 0.30 and SSF < 4.

Juxtaposition and membrane-seal diagrams

To develop an understanding of how the faults within the Aurora storage site may influence the migration of injected CO_2, we assessed the presence of juxtaposition seals and membrane seals. The SGR algorithm was favoured over SSF for creating the membrane-seal diagrams because it considers clay contributions for a wider range and enables comparison with previous studies (i.e. Bretan *et al*. 2011; Bretan 2017; Osmond *et al*. 2022). We focus again on the Svartalv 2, F1 and F3 faults (Fig. 10). Due to the dip of the storage units (Fig. 4a), migrating CO_2 injected at or near well 31/5-7 is likely to encounter the first-order Svartalv 2 in the footwall side over time. As shown in Figure 6, Svartalv 2 exhibits throw exceeding the thickness of the primary seal (>85 m: Fig. 4b), and consequently offsets the storage complex along the northern segment of the fault. Furthermore, it is intersected by multiple faults (e.g. F3 and F4), which cause throw variations along strike and influence the arrangement of juxtaposed hanging-wall units against the storage-complex interval (Fig. 10a). At the southern tip of Svartalv 2, both the primary and secondary storage units are mainly self-juxtaposed. As the throw increases northwards, the secondary storage in the footwall becomes juxtaposed against the primary seal in the hanging wall, creating a juxtaposition seal. Further north, the throw exceeds the thickness of the primary seal (>85 m), and both storage units in the footwall become juxtaposed against younger and potentially sand-rich units in the hanging wall (overlying units herein). Along the northern part of Svartalv 2, the throw decreases, and the lower parts of the primary storage unit in the footwall become juxtaposed against the secondary storage unit in the hanging wall. Due to the presence of a thin (herein modelled with a constant thickness of 22 m) Upper Amundsen Formation, a juxtaposition seal could be present within the uppermost parts of the primary storage unit for throws below *c.* 22 m (i.e. northernmost and southernmost fault tips). The SGR diagrams for the first-order Svartalv 2 show that, in areas where the two storage units in the footwall become juxtaposed against overlying units in the hanging wall, SGR values generally exceed 0.30–0.40 (Fig. 10b). The highest SGR values (>0.40) are present where the uppermost secondary storage unit in the footwall is juxtaposed against overlying units in the hanging wall. The SGR values then decrease downsection to <0.20 at −2245 m TVDSS within the primary storage unit on the footwall side (Fig. 10b). Where the primary storage unit in the footwall is juxtaposed against the secondary storage unit in the hanging wall, SGR values are generally <0.15. However, the Upper Amundsen Formation contributes slightly higher SGR values (>0.15) in the uppermost part of the secondary storage unit, as predicted from the triangle diagrams in Figure 9a, c.

The second-order F1 and F3 faults are dipping towards the east and the NE, respectively (Fig. 5b). Thus, well 31/5-7 is located in the footwall of both faults. F1 and F3 have throws less than the thickness of the primary seal (i.e. <85 m: Figs 7 and 8) and do not juxtapose the storage units against overlying potentially sand-rich units (Fig. 10a). For both faults, parts of the primary storage unit in the footwall are juxtaposed against the lower parts of the secondary storage unit in the hanging wall. For low throws, the primary storage unit in the footwall is juxtaposed against the inferred Upper Amundsen Formation in the hanging wall. Furthermore, the upper parts of the primary storage unit in the footwall are juxtaposed against the primary seal in the hanging wall, potentially creating a juxtaposition seal. As we present in Figure 8b, the second-order F3 fault interacts with Svartalv 2 in the footwall and, as a consequence, a 28 m-high juxtaposition seal is present at the top of the secondary storage unit where the two faults intersect. The SGR diagrams for F1 and F3 show that where the primary storage unit in the footwall is juxtaposed against the secondary storage unit in the hanging wall, the calculated SGR values generally range between 0.15 and 0.20 (Fig. 10b). Higher SGR values (>0.15) are also observed where the secondary storage unit is self-juxtaposed, potentially due to the thickening of the Upper Amundsen Formation towards the north in well 31/5-2 (Fig. 9b).

Based on our observations, we made generalized juxtaposition and membrane-seal scenarios for all interpreted faults displacing the top primary and secondary storage unit (Fig. 11). From Figure 11a, it is evident that most second-order faults exhibit sandstone on sandstone juxtapositions at the top of the primary storage unit. An exception is present where the upper parts of the primary storage unit in the footwall of east- and NE-dipping second-order faults are juxtaposed against the inferred Upper Amundsen Formation in the hanging wall in areas with low throw values (i.e. near the fault tips: Fig. 10a). The east- and NE-dipping second-order faults generally have SGR values ranging from 0.15 to 0.20 at the top of the primary storage unit (Fig. 10b). However, due to the northward thickening of the Upper Amundsen Formation (Fig. 9), east- and NE-dipping second-order faults are envisaged to have higher SGR values, predominately in the range 0.20–0.40, towards the north (Fig. 11a).

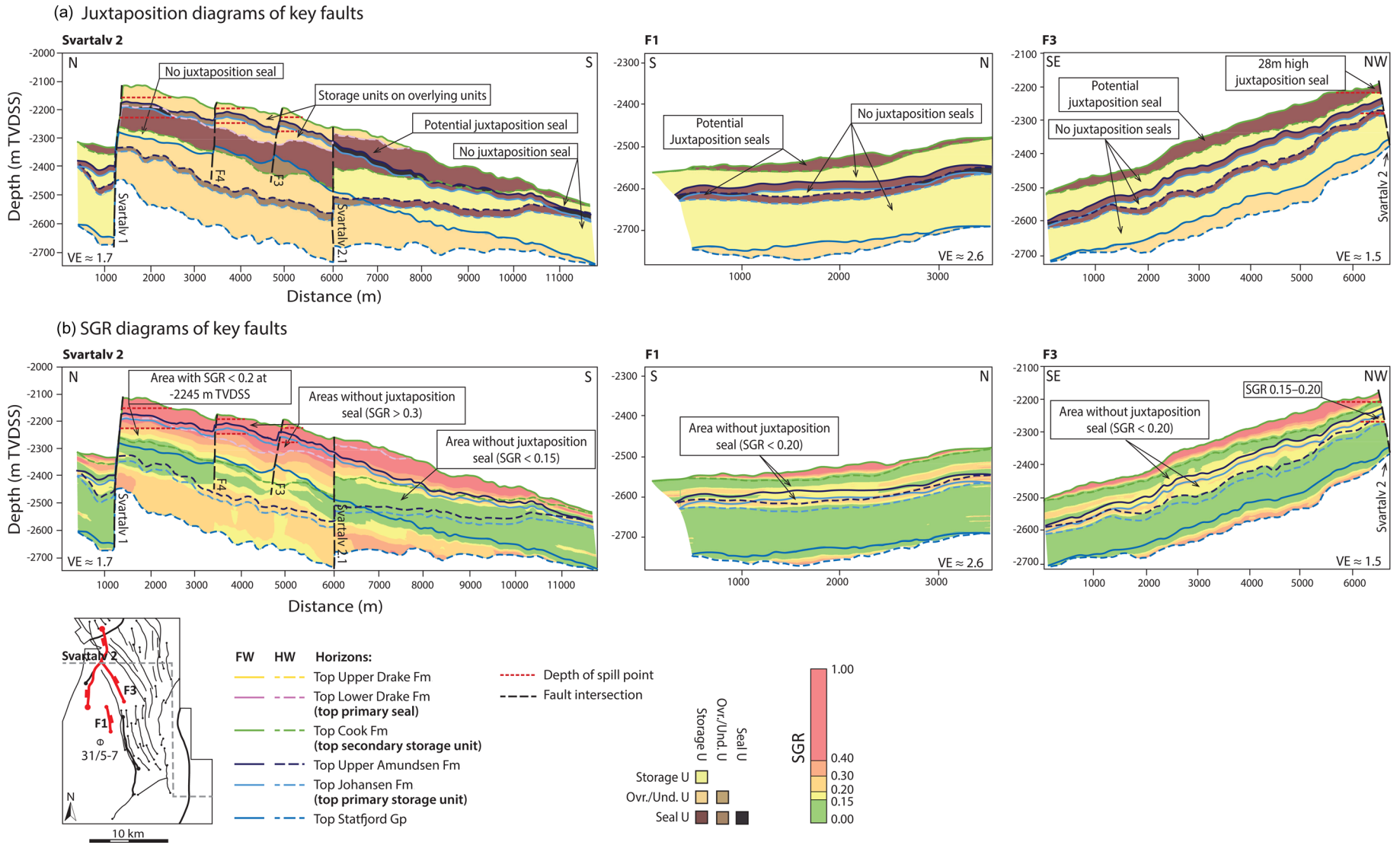

Fig. 10. Allan diagrams showing a close-up of storage-complex horizon cutoff lines and fault intersections present along faults shown in Figures 6–8. The Allan diagrams are populated with (**a**) juxtaposition scenarios and (**b**) calculated shale gouge ratio (SGR), derived from wells 31/5-7, 31/2-5 and 31/5-2 (Fig. 9); values are viewed from the hanging-wall side. Spill points of potential structural traps (see Fig. 12; Table 1) are indicated with a red stippled line. See Figure 5b for a complete overview of the faults that intersect Svartalv 2 in the footwall. The inset shows the location of the faults and their dip direction relative to well 31/5-7 (Eos). Footwall cutoff lines are indicated with solid lines, and hanging-wall cutoff lines with dashed lines. The location of the Upper Amundsen Formation is inferred based on the average thickness determined from wells 31/5-7, 31/5-2 and 31/2-5 (22 m). VE, vertical exaggeration; HW, hanging wall; FW, footwall; Storage U, storage units; Ovr./Und. U, overlying and underlying units; Seal U, seal unit.

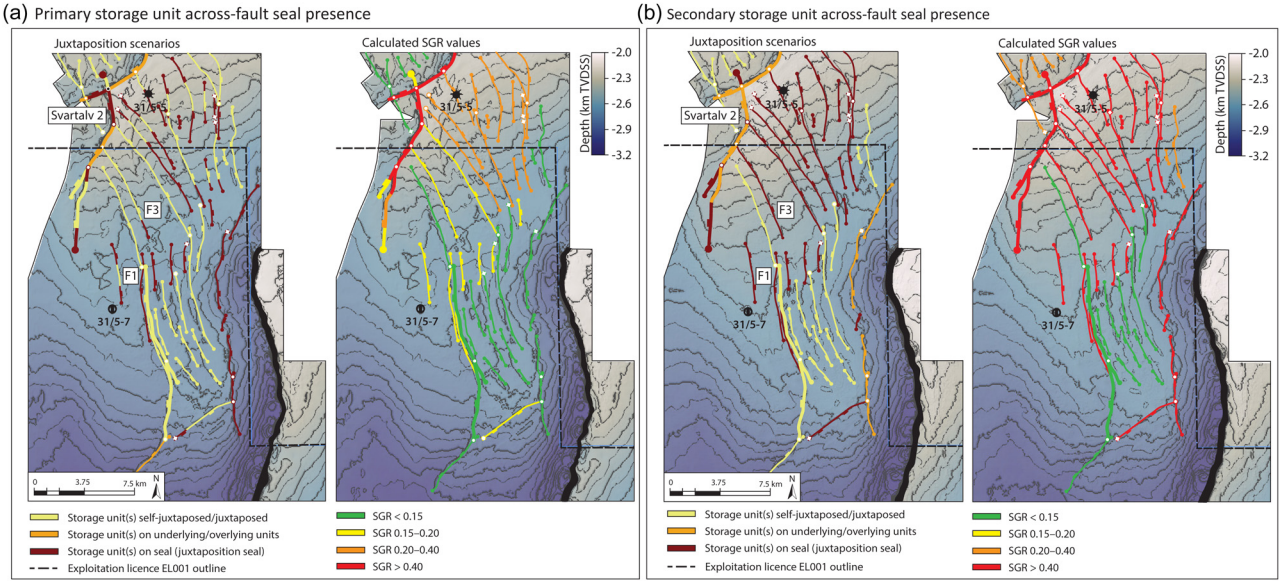

Fig. 11. The generalized presence of across-fault seals in the upper parts of (**a**) the primary storage unit and (**b**) the secondary storage unit provided injection at or near well 31/5-7. Maps illustrate the presence of across-fault seals for the uppermost parts of the storage units based on detailed across-fault seal assessment (Fig. 10a), observations from shale gouge ratio (SGR) triangle diagrams (Fig. 9), throw v. distance profiles for F1 and F3 (Figs 7, 8), and the compilation of maximum throw measurements in Appendix A. The SGR cutoff values in (b) are based on the calibration in Yielding (2002). Faults are displayed on a depth–structure map of the top secondary and primary storage units with a contour spacing of 50 m TVDSS. The scientific colour bar (version 7.0.0) is sourced from Crameri (2021).

The west- and SW-dipping second-order faults generally exhibit sandstone on sandstone juxtapositions with SGR < 0.15 (Fig. 11a). These faults do not have throw exceeding the thickness of the primary storage unit (*c.* 140 m), which would juxtapose the top of the primary storage unit in the hanging wall against underlying units (i.e. the Statfjord Group) in the footwall.

At the top of the secondary storage unit (Fig. 11b), multiple east- and NE-dipping second-order faults create juxtaposition seals (Figs 10a and 11b). In contrast, west- and SW-dipping second-order faults create sandstone on sandstone juxtapositions with SGR < 0.15 (Fig. 10). However, due to the secondary storage unit becoming thinner and more heterogeneous northwards (Fig. 9), higher SGR values, predominately in the range 0.20–0.40, are envisaged for west- and SW-dipping second-order faults in the northern part of the study area. For both storage units, the Svartalv Fault Zone (herein Svartalv 1, Svartalv 2 and Svartalv 2.1) exhibits varying juxtaposition scenarios. In areas of maximum displacement, the Svartalv Fault Zone juxtaposes the top of the storage units in the footwall against the overlying units in the hanging wall. However, calculated SGR and SSF values are generally >0.40 and <4, respectively, in these areas (Figs 9 and 10b).

Structural traps

Fault-bound traps are present north of well 31/5-7 where NE-dipping second-order faults (i.e. F3 and F4) are hard-linked to the first-order Svartalv 2 fault, and where the first-order Svartalv 1 and Svartalv 2 faults cross-cut each other (Fig. 5b). These three structural traps are located 9.9, 11.4 and 13.7 km north of well 31/5-7, respectively, and represent areas where CO_2 could accumulate (Fig. 12) provided that they create effective across-fault seals (i.e. juxtaposition or membrane seals) for CO_2 migration (discussed below). It is, therefore, of interest to assess the GRV of these traps. The first structural trap is located where the second-order F3 fault is hard-linked with Svartalv 2 (Fig. 12). Because F3 exhibits lower throw values compared to Svartalv 2, the height of the corresponding structural trap is limited to the throw of F3 at the depth of the primary and secondary storage units, which are 31 and 28 m, respectively (Table 1). Based on these heights and the overall dip of the storage unit depth–structure maps (southwards: Fig. 4a), the calculated GRV is 9.1×10^6 m^3 in the primary storage unit and 1.5×10^6 m^3 in the secondary storage unit (Table 1). The second structural trap is located where F4 is hard-linked with Svartalv 2 (Fig. 12). Similar to the first structural trap, the height of the structural traps are 23 and 24 m for the primary and secondary storage units, respectively, because they are limited by their throw along F4 (Table 1). These heights equate to a GRV of 5.0×10^6 m^3 in the primary storage unit and 2.9×10^6 m^3 in the secondary storage unit. The third structural trap is located where Svartalv 2 and Svartalv 1 are hard-linked (Fig. 12). Here, the height of the trap in both storage units is 48 m (Table 1). These heights equate to a GRV of 94×10^6 m^3 in the primary storage unit and 60×10^6 m^3 in the secondary storage unit, which are the largest within the study area along the possible CO_2 migration pathway (Table 1). Overall, these structural traps have a combined GRV of 108×10^6 m^3 in the primary storage unit and 64.4×10^6 m^3 in the secondary storage unit.

Discussion

We used the GN10M1 merged 3D seismic survey and well data to create a high-resolution interpretation of the storage complex and the intersecting faults within the Aurora storage site. Our interpretations provide insights into the structural evolution of the Aurora storage site, across-fault seal presence, trapping and influence over CO_2 migration.

Structural evolution and fault linkage

The synthesis of thickness maps, throw v. depth profiles and expansion index profiles reveals the timing of fault nucleation and subsequent periods of reactivity within the Aurora storage site. In turn, our findings supplement recent studies from the Smeaheia fault block (Bell *et al.* 2014; Mulrooney *et al.* 2020; Wu *et al.* 2021), the Troll West and East fields (Whipp *et al.* 2014; Duffy *et al.* 2015), and the Oseberg Field (Deng *et al.* 2017), allowing us to compare their structural evolution with that of the Aurora storage site. Sizable

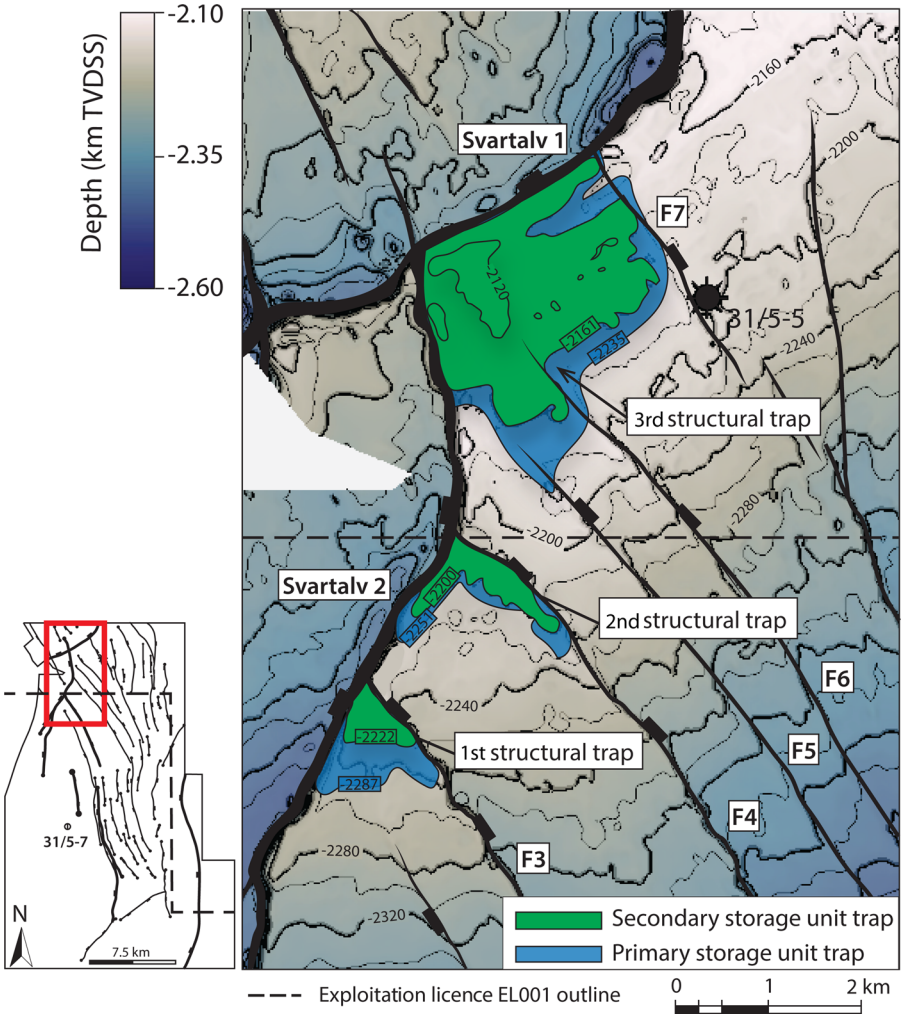

Fig. 12. Close-up of primary and secondary storage unit structural traps (blue and green, respectively) interpreted updip of well 31/5-7 and displayed on the top secondary storage unit depth–structure map. Contour interval spacing is 20 m (bolded every 40 m starting at −2160 m TVDSS). The depth of the spill point compiled in Table 1 is illustrated for each trap. Note that the structural trap outlines and spill points in the primary storage unit do not conform to the depth–structure map of the secondary storage unit. The scientific colour bars (version 7.0.0) are sourced from Crameri (2021).

throw magnitudes (up to 550 m TVDSS) and hanging-wall expansion (EI between 1.13 and 1.6) observed from the Svartalv 2 fault are generally consistent with observations from the Troll West Field (Whipp *et al.* 2014; Duffy *et al.* 2015) and for first-order faults overall in the Horda Platform (e.g. Bell *et al.* 2014). It is important to note that Upper Jurassic hanging-wall expansion is likely to be exaggerated due to the erosion of the Upper Jurassic Draupne Group in the footwall of the Svartalv Fault Zone (Whipp *et al.* 2014). However, we also observe expansion (EI of 1.17) for Lower Jurassic units along Svartalv 2 and Svartalv 1 (Figs 4b and 6c), suggesting that reactivation of the southern segments of the Svartalv Fault Zone occurred before reactivation of the fault zone further north. These findings are consistent with Lower Jurassic fault activity observed in the Oseberg Field (Færseth and Ravnås 1998; Deng *et al.* 2017) and the overall diachronous nature of Rift Phase 2 in the North Sea (Bell *et al.* 2014; Mulrooney *et al.* 2020). While no obvious wedge-shaped geometries are visible across the second-order faults in our study area, some hanging-wall expansion is observed in the Upper Jurassic–Cretaceous units for F1 and F3 (Figs 7c and 8c), which is likely to indicate nucleation during Rift Phase 2. The maximum throw values for F1 and F3 are located in the Upper Triassic and Lower Jurassic units, indicating that the burial depth at the time of fault nucleation was <1 km. This shallow depth promotes the formation of disaggregation and, perhaps, subordinate cataclastic deformation bands in clay-poor sequences (e.g. where storage units are self-juxtaposed) (Fisher and Knipe 2001; Sperrevik *et al.* 2002; Fossen *et al.* 2007), although significant uncertainty is associated with the formation depth of various deformation band types (e.g. Braathen *et al.* 2018*a*). Lower-order throw maxima are present for F1 and F3, suggesting either reactivation or vertical linkage (i.e. dip linkage) of individual faults. Overall, our observations of fault evolution of second-order faults within the Aurora storage site correlate well with observations made in the Troll West Field (Whipp *et al.* 2014; Duffy *et al.* 2015).

Table 1. *Compilation of the depth to the crest of the trap, depth to the spill point, height of the trap, gross rock volume (GRV) and across-fault seal types of the individual structural traps interpreted from the primary and secondary storage units as illustrated in Figure 12*

Structural trap	Storage unit	Crest of trap (m TVDSS)	Spill point (m TVDSS)	Height of the trap (m)	GRV ($\times 10^6$ m)	Faults that define the structural trap
First	Primary	−2256	−2287	31	9.1	Svartalv 2/F3
	Secondary	−2194	−2222	28	1.5	Svartalv 2/F3
Second	Primary	−2228	−2251	23	5.0	Svartalv 2/F4
	Secondary	−2176	−2200	24	2.9	Svartalv 2/F4
Third	Primary	−2187	−2235	48	94	Svartalv 2/Svartalv 1
	Secondary	−2113	−2161	48	60	Svartalv 2/Svartalv 1

Throw v. length profiles for Svartalv 2, F1 and F3 (Figs 6b, 7b and 8b) provide an insight into local fault interactions. The Svartalv 2 segment shows a step-like throw profile within the Lower–Middle Jurassic units. Steps that correlate with areas of fault interaction suggest hard-linkage (e.g. F3, F4 and Svartalv 1), whereas smaller steps that do not correlate with the interaction of nearby faults are likely to be a result of segmentation and linkage of the Svartalv 2 fault (Fig. 6b). Evidence of hard-linkage is also apparent from the throw v. length profile for F3, where throw gradients are significantly steeper towards the NW and the intersection with Svartalv 2. Steps in throw as a result of hard-linkage with second-order faults are only present in the footwall and suggest that the lateral propagation of second-order faults were impeded by the pre-existing Svartalv 2 fault during Rift Phase 2. Further rifting and extension during Rift Phase 2 led to the accumulation of mutual throw magnitudes at points where they intersect. In contrast to F3, F1 shows a near symmetrical throw v. length profile, indicating that the fault grew with little interaction with nearby faults.

Overall, half of all second-order faults in the Aurora storage site are soft-linked or hard-linked to the pre-existing first-order faults or other second-order faults (Fig. 5b). This observation aligns well with interpretations from the Troll West Field by Duffy *et al.* (2015). Furthermore, the observation that second-order faults appear to have been influenced by the presence of pre-existing first-order faults suggests that the first-order faults have acted as strain barriers, thus restricting the lateral propagation of the second-order faults in accordance with the findings of Henza *et al.* (2010) and Duffy *et al.* (2015). In general, we find that fault linkage is abundant within the Aurora storage site, which will likely influence the migration of injected CO_2.

Across-fault seal presence

The structural and stratigraphic architecture and across-fault seal assessment we have presented above provide a framework in which we can discuss our confidence in across-fault seal presence within the Aurora storage site. Due to the overall dip of the storage units, we assume that buoyant CO_2 injected at or near the location of well 31/5-7 rises to the top of the porous and permeable storage units and migrate updip towards the north. Faults within this projected updip CO_2 migration path are characterized by variable across-fault seal types where they displace the storage units (Figs 10 and 11).

While both juxtaposition seals and membrane seals can provide effective traps and baffles in hydrocarbon fields (e.g. Knott 1993; Fristad *et al.* 1997; Yielding 2002; Lyon *et al.* 2005; Færseth *et al.* 2007; Childs *et al.* 2009), significant uncertainties are related to the assessment of such seals in the subsurface. Juxtaposition seals are generally considered to have the highest probability of sealing (e.g. Færseth *et al.* 2007); however, subseismic fault-zone complexities may influence the across-fault connectivity, making it challenging to accurately predict the sealing potential (e.g. Childs *et al.* 1997; Færseth *et al.* 2007). Generally speaking, membrane seals are considered to have a lower probability of sealing compared to juxtaposition seals (Færseth *et al.* 2007). This is partly due to uncertainties in applying well data as a proxy for fault-rock composition (Yielding *et al.* 2010). Moreover, the wetting properties of a CO_2–brine–rock system, which defines the fault-seal capacity in a two-phase fluid system, are a source of uncertainty (e.g. Iglauer *et al.* 2015; Miocic *et al.* 2019; Karolytė *et al.* 2020). Miocic *et al.* (2019) suggested that because of a preferred CO_2 wettability of clay minerals, higher entrainment of clay into the fault rock may in fact reduce the amount of CO_2 that can be securely retained. Finally, the presence of deformation bands, such as disaggregation and cataclastic bands in sand-rich units, has been found to have a baffling effect on fluid migration (Fisher and Knipe 2001). However, the influence of such deformation bands on fluid migration is ambiguous as they may also form conduits for fluid migration (Braathen *et al.* 2018*a*).

Considering these uncertainties, our confidence in across-fault seal presence within the Aurora storage site can be subdivided into four categories (Fig. 13a). We are least confident that self-juxtaposition or juxtaposition of sand-rich storage units with SGR < 0.20 will form effective seals (category 1). It is, however, important to note that because deformation bands are not accounted for in classic fault-seal algorithms such as SGR, our predictions for sandstone on sandstone juxtaposition may be somewhat conservative. Higher SGR values increase our confidence that an across-fault seal is present. Based on the calibration by Yielding (2002), we relate lower confidence to faults with SGR values ranging from 0.20 to 0.40 (category 2) compared to faults with SGR > 0.40 (category 3). Finally, we are most confident that juxtaposition seals will provide effective seals within the Aurora storage site (category 4).

When we apply these categories to the interpreted faults north of well 31/5-7, we find that, at the top of both storage units, we have generally low confidence that west- and SW-dipping second-order faults will provide effective seals for CO_2 migration (categories 1 and 2: Fig. 13b). As presented above, lateral variations in the clay content are present due to the thickening of the Upper Amundsen Formation towards the north (Figs 9 and 11). Consequently, we have somewhat higher confidence in the across-fault seal potential for east- and NE-dipping second-order faults that displace the primary storage unit towards the north (category 2) compared to those closer to well 31/5-7 (category 1: Fig. 13b). For the secondary storage unit, we have higher confidence (category 4) that east- and NE-dipping second-order faults will form effective across-fault seals for CO_2 migration, compared to the primary storage unit (categories 2 and 4: Fig. 13b). The Svartalv Fault Zone (herein Svartalv 1 and 2) displays along-strike variations in across-fault seal presence (Fig 10a, b), and we are slightly more confident in the presence of effective across-fault seals at the top of the secondary storage unit than in the case of the primary storage unit (Fig. 13b).

In general, we observe that areas showing SSF < 4 often correlate with those exhibiting SGR > 0.30–0.40 in our models (Fig. 9), suggesting that a continuous smear is present, and supports our confidence in across-fault seal potential where the Svartalv Fault Zone juxtaposes storage units in the footwall against overlying units in the hanging wall. However, in places where SGR < 0.30, SSF values are generally higher than 4 (Fig. 9), suggesting that the smear has potential discontinuities or is not continuous where east- and NE-dipping second-order faults juxtapose the primary storage unit in the footwall against the secondary storage unit in the hanging wall. Direct sampling of well cores and image log analysis are beyond the scope of this study, and, therefore, we cannot determine whether the membrane seal consists of abrasion-type shale smear or more ductile clay smear. However, the correlation between calculated SGR values and SSF values suggests that our confidence in across-fault potential for second-order faults is somewhat lowered compared to the first-order Svartalv Fault Zone (Fig. 13). Overall, considering all the contributions discussed herein, we have a higher level of confidence in the presence of across-fault seals at the top of the secondary storage unit and generally a higher level of confidence in across-fault seal potential towards the north for both storage units.

Plausible CO_2 migration routes

Considering that the primary seal unit exhibits a relatively tabular thickness with few signs of thinning or erosion within the study area (Fig. 4b), we suggest that vertical migration through the primary seal is unlikely. This is further supported by geomechanical and petrophysical studies of the Drake Formation indicating that it serves as an effective seal in Aurora (Rahman *et al.* 2022*a*, *b*).

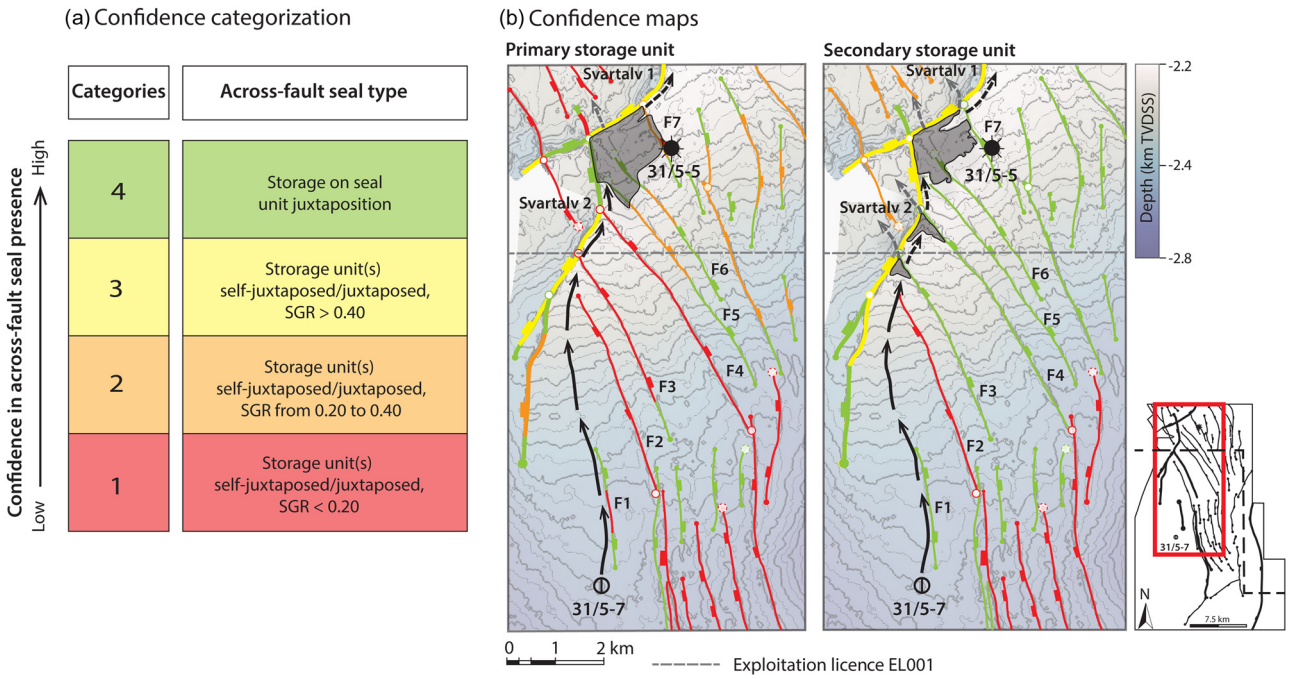

Fig. 13. (**a**) Confidence scheme for the across-fault seal presence subdivided into four categories from low to high confidence. The categorization is inspired by Færseth *et al.* (2007), Miocic *et al.* (2019) and Karolytė *et al.* (2020). (**b**) Maps showing faults within the projected updip CO_2 migration pathway colour-coded based on the categorization scheme shown in (a) and displayed on the top depth–structure maps for the primary and secondary storage units. The contour interval spacing is 20 m (bolded every 40 m starting at −2200 m TVDSS). Plausible CO_2 migration pathways are drawn perpendicular to the contour lines, and are illustrated with black and grey arrows Structural traps are indicated with a solid black outline. Solid lines represent more plausible migration routes compared to dashed lines, and black lines represent more favourable migration routes in terms of storage integrity and capacity compared to those in grey.

However, the across-fault seal presence updip of well 31/5-7 will be likely to influence the migration of injected CO_2. Therefore, our confidence map can also be used to discuss plausible migration routes and GRVs in a fill-to-spill scenario given injection at or near well 31/5-7 (Fig. 13b).

Injected CO_2 is likely to eventually encounter several NW–SE-orientated second-order faults and the first-order Svartalv Fault Zone (herein modelled as Svartalv 1 and 2) on its footwall side (Fig. 13b). In the primary storage unit, we are more confident that Svartalv 2 forms effective across-fault seals (category 3) compared to the NW–SE-striking and NE-dipping second-order faults F3 and F4 (category 1). As a result, we suggest that the CO_2 plume will be most likely to migrate northwards into the footwall of Svartalv 2 without accumulating within the first and second structural traps mapped in Figure 12. It is important to note that migration within the primary storage unit also relies on the Upper Amundsen Formation serving, more or less, as an effective flow barrier. While recent studies suggest that it is likely to slightly retard but not severely inhibit vertical migration between the two storage units (Meneguolo *et al.* 2022), a lack of well control within the predicted northward-migration route makes it challenging to know the lateral variations in thickness and lithology, and their influence on CO_2 migration. Nevertheless, because faults F3 and F4 juxtapose the primary storage unit against the secondary storage unit (Fig. 10), we have low confidence in the presence of across-fault seals (category 1: Fig. 13a), implying that injected CO_2 will migrate from the primary to the secondary storage unit as it encounters these faults (Fig. 13b). Therefore, we predict that most of the CO_2 injected into the primary storage unit will reach the secondary storage unit simply due to the current structural architecture of the storage complex.

If any CO_2 remains in the primary storage unit, it will eventually reach the third structural trap formed by Svartalv 1 and 2 (Fig. 12). For Svartalv 2, a juxtaposition seal (category 4) is present from the crest of the trap to the spill point for the primary storage unit (Figs 10 and 13b). Below *c.* −2245 m TVDSS, 10 m below the depth of the spill point in the primary storage unit (Fig. 10), SGR values are less than 0.20 and across-fault migration is plausible. However, due to the overall southward dip of the storage units (Figs 4 and 12), accumulating CO_2 would be likely to spill northeastwards into the Troll West Field before the base of the CO_2 column reaches this depth. The utility of the third trap also relies on the presence of an effective membrane seal for Svartalv 1. While there are uncertainties related to assessing the presence of membrane seals, our findings suggest that SGR values are generally above 0.30–0.40 where storage units are juxtaposed against overlying units (Fig. 9) and, therefore, we have relatively high confidence in the presence of an effective membrane seal across Svartalv 1.

Previous studies by Bretan *et al.* (2011) and Osmond *et al.* (2022) present detailed Allan diagrams for the Svartalv Fault Zone (herein referred to as Svartalv 1), and conclude that SGR values are generally in the range 0.20–0.30 where the storage units are juxtaposed against overlying units across Svartalv 1 (category 2). Interestingly, Osmond *et al.* (2022) found that even though hydrocarbon production is causing regional pressure depletion in the overlying Upper Jurassic Viking Group sandstones at the Troll and Brage fields (Fig. 1b), formation pressure within the Lower Jurassic primary and secondary storage units remains at unaltered hydrostatic conditions despite large contacts where they are juxtaposed against the producing Upper Jurassic sandstones along first-order faults within the northern Horda Platform. Their modelling indicates that SGR values of 0.15 or greater correlated with across-fault pressure differentials (AFPD) of >20 bar along the Vette Fault Zone, suggesting that an across-fault membrane seal is present at these critical sandstone on sandstone juxtapositions. While they were unable to confirm the same observation with pressure data, they inferred that membrane seals were also probable at Lower Jurassic on Upper Jurassic sandstone juxtapositions along the Svartalv Fault Zone because SGR values were also >0.15. Their observations show the utility of the SGR algorithm and are

significant for our study at Aurora because although SGR > 0.40 may signify high-confidence membrane-seal areas (category 3) as an empirical rule (i.e. Bretan *et al*. 2003; Yielding *et al*. 2010), membrane seals may still be present along the Svartalv 1 fault and other faults within our study area where SGR values are between 0.15 and 0.40 (categories 1 and 2). However, formation pressure data from both sides of the Svartalv Fault Zone acquired after the start of hydrocarbon production in Upper Jurassic sandstones are necessary to further de-risk membrane-seal presence.

With respect to the secondary storage unit, NE-dipping and NW–SE-striking second-order faults will be likely to provide small (24–48 m: Table 1) juxtaposition seals (category 4) within the upper parts of the storage units and channel the injected CO_2 towards the footwall of Svartalv 2 (i.e. northwestwards: Fig. 13b). In the secondary storage unit, the Svartalv 2 exhibits SGR values exceeding 0.40 from the crest of the trap to the spill point, indicating that a membrane seal (category 3) is present (Yielding 2002). We suggest, therefore, that it is more likely that CO_2 will become trapped within the first and second structural trap if the plume resides within the secondary storage unit compared to the primary storage unit (Fig. 13b). However, the presence of these structural traps could temporarily inhibit or prevent CO_2 from migrating northeastwards, thereby increasing the buoyancy pressure of CO_2 against the Svartalv 2 fault. Therefore, structural traps potentially represent areas with a higher risk of migration across the Svartalv Fault Zone and into overlying and potentially sand-rich units, such as the upper parts of the Drake Formation and the Brent Group (Fig. 13b).

Overall, we favour northward migration within the Svartalv fault block (Svartalv Fault Zone footwall) in both storage units (Fig. 13b). This migration route prevents escape out of the intended storage units, as it only encounters second-order faults that do not offset the storage units. Furthermore, it allows CO_2 to accumulate within smaller-scale structural traps, which slows down plume migration and allows CO_2 to also become trapped due to residual, solubility and mineral trapping (Benson and Cole 2008), thus increasing the storage capacity. Provided that CO_2 remains in the footwall of the Svartalv Fault Zone, it will be likely to migrate north and out of our study area, stratigraphically segregated about 500 m below the hydrocarbon-bearing units of the Troll Field (Fig. 13b). Previous studies by Bretan *et al*. (2011) and Osmond *et al*. (2022) show that the throw of the Svartalv Fault Zone increases north of our study area, and that the fault juxtaposes storage units against the Brent Group and the hydrocarbon-bearing sandstones of the Viking Group but suggest across-fault seal presence.

Based on our assessment, we support injection of CO_2 into the primary storage unit as established by Furre *et al*. (2020), using an inclined or semi-horizontal well to increase the migration route and reduce the mobility of the CO_2 plume (Sundal *et al*. 2015). In addition, it will be likely to allow CO_2 to migrate into the secondary storage unit, where we have higher confidence in the structural trapping potential (Fig. 13b). Assuming that the onset of membrane seals occurs when SGR > 0.20 (Bretan *et al*. 2003; Yielding *et al*. 2010) and juxtaposition seals prevent across-fault migration, the total GRV of structural traps is 94×10^6 m^3 in the primary storage unit and 64.4×10^6 m^3 in the secondary storage unit. Previous studies of GRV, using SGR > 0.20 to represent potential across-fault seals, by Bretan *et al*. (2011) and Osmond *et al*. (2022) observed similar volumes in the Troll Field, which increases the storage capacity of the Aurora storage site as the CO_2 plume migrates northwards. It is important to note, however, that the maximum CO_2 column height retained by a membrane seal, in particular for SGR values between 0.20 and 0.40, is not necessarily confined to the height of structural traps but also depends on whether the buoyancy pressure of accumulated supercritical CO_2 exceeds the capillary entry pressure of the fault rock (e.g. Bretan *et al*. 2003; Manzocchi *et al*. 2010). Estimates of membrane-limited CO_2 column heights in the Troll West Field by Bretan *et al*. (2011) suggest that faults with SGR values exceeding 0.25 can hold a CO_2 column height of 100 m. If we apply these estimates to the Aurora storage site, Svartalv 2 and 1 can retain the column heights of the structural traps (i.e. 24–48 m: Table 1). However, the methodology applied in Bretan *et al*. (2011) was originally developed based on hydrocarbon column heights juxtaposed against sealing faults observed in hydrocarbons fields and does not consider the uncertainties related to fault-seal parameters for CO_2 (i.e. wettability properties, fault rock composition and reservoir depth on retention potential). Miocic *et al*. (2019) and Karolytė *et al*. (2020) suggested that applying these methods directly to CO_2 storage sites without modification can, therefore, provide erroneous results. To increase our confidence in the migration routes and storage capacity within the Aurora storage site, it will be necessary to develop new methods that provide more accurate calculations of fault capacity in CO_2 storage sites.

Furthermore, it is important to note that our study solely focuses on the presence and influence of across-fault seals on the migration of CO_2 within the Aurora storage site. It does not consider the potential of injected CO_2 to cause stress-induced reactivation of faults, breach of potential seals or upfault migration (e.g. Jones and Hillis 2003; Lyon *et al*. 2005; Osmond and Meckel 2020). Due to the variations in strike of faults within Aurora (Fig. 5b), it could be argued that some faults are orientated more favourably for reactivation. However, previous studies within the Troll Field (Bretan *et al*. 2011), the Smeaheia storage site (Skurtveit *et al*. 2018; Rahman *et al*. 2021) and the Aurora storage site (Nedberg 2022) suggest that there is an overall low risk of reactivation as a consequence of CO_2 injection in a normal stress regime. In addition, fault-linkage zones may represent areas with an increased risk of both upfault and across-fault migration due to more complex deformation (e.g. multiple slip planes, wider damage zone, fracturing of the seal and relay ramps: e.g. Childs *et al*. 1997; Manzocchi *et al*. 2010; Fossen and Rotevatn 2016). While this is beyond the scope of our study, a detailed assessment of fault linkage and influence on upfault migration is needed to further de-risk the Aurora storage site. Nevertheless, our confidence map can be utilized to highlight areas away from the injection well where monitoring may be beneficial. For example, along the Svartalv Fault Zone where second-order faults are hard-linked in the footwall (Fig. 13b). Outside of the Aurora storage site, a similar assessment of across-fault seal confidence could be generated to assess other CO_2 storage sites in the future.

Conclusions

Injection of CO_2 within the Aurora storage site is scheduled to commence in 2024 with injection at or near well 31/5-7 in the northern North Sea. To improve our geological understanding of the storage site and discuss the potential impact of faults on the migration of injected supercritical CO_2, we created a structural geomodel of the Aurora storage site, described structural features and assessed the presence of across-fault seals. Our main findings and recommendations are summarized as follows:

- The storage complex within the Aurora storage site comprises two Lower Jurassic storage units and an overlying seal. The storage complex dips gently (*c*. 2°) towards the south and shallows northwards towards the Troll licence. The primary and secondary storage units have an average thickness of 130 and 30 m, respectively. The primary seal exhibits a relatively tabular thickness of 85 m within the study area and shows little signs of thinning.

- Two fault populations displace the storage complex. First-order faults, which displace the basement–cover contact, are predominately north–south striking and exhibit throw maxima ranging from 43 to 940 m. Second-order faults are generally NW–SE- to north–south-orientated, have no preferred dip direction and are largely restricted to the Upper Triassic–Cretaceous units, with throws ranging from 15 to 50 m.
- Fault formation coincides with Permian–Triassic rifting. Reactivation of the southern parts of the Svartalv Fault Zone likely occurred during the Early Jurassic. Second-order faults likely formed due to Late Jurassic to Early Cretaceous rifting at relatively shallow depths (<1 km).
- Second-order NW–SE-striking faults exhibit steep throw v. distance gradients towards the footwall of the Svartalv Fault Zone, and, in places, link up and form structural traps within the projected updip migration pathway for CO_2. These traps possess a combined GRV of 158×10^6 m^3 for both storage units. In a fill-to-spill scenario, buoyant supercritical CO_2 is likely to accumulate in these traps, contributing to the overall trapping capacity.
- Second-order faults within the Svartalv fault block generally have throws less than the thickness of the primary seal (<85 m) and, as a result, migration out of the storage units is unlikely. However, east- and NE-dipping second-order faults form juxtaposition seals within the upper parts of the secondary storage unit, which are likely to create local side seals for CO_2 migration. Furthermore, they juxtapose the primary storage unit in the footwall against the secondary storage unit in the hanging wall, allowing CO_2 to migrate into the secondary storage unit. In contrast, west- and SW-dipping second-order faults are likely to allow across-fault migration within the storage units.
- Injected CO_2 is likely to encounter the first-order Svartalv Fault Zone in the footwall, which juxtaposes both storage units against overlying units in the hanging wall. However, membrane-seal assessment shows that the calculated SGR values generally exceed 0.30, potentially preventing this scenario of across-fault migration.
- Injection of CO_2 into the primary storage unit will increase the length of the migration route by allowing CO_2 to migrate from the primary storage unit to the secondary storage unit, where we have higher confidence in across-fault seal presence across NE-dipping second-order faults. This migration route will also slow down migration thereby allowing more CO_2 to become trapped due to structural, residual, solubility and mineral trapping. Furthermore, areas where second-order faults link up with the Svartalv Fault Zone in the secondary storage unit potentially represent areas with a higher risk of across-fault migration.

Acknowledgements The authors acknowledge the following partners for their contributions: Aker Carbon Capture, Allton, Ansaldo Energia, Baker Hughes, CoorsTek Membrane Sciences, Equinor, Fortum Oslo Varme, Gassco, KROHNE, Larvik Shipping, Lundin Norway, Norcem, Norwegian Oil and Gas, Quad Geometrics, Stratum Reservoir, TotalEnergies, Vår Energi and Wintershall DEA. The workflows herein were conducted in collaboration with the Northern Lights JV DA (Equinor, Total and Shell). We gratefully acknowledge Schlumberger for the provision of academic licences for the Petrel E&P Software Platform, and Petroleum Experts for the provision of academic licences for the Move Software Suite. Gassnova SF provided access to the GN10M1 3D seismic survey. The authors also wish to thank the editorial team, Frauke Schaefer and an anonymous reviewer for critically assessing the manuscript, as well as Emma Michie for creating the velocity model and Sian Evans for helpful comments.

Author contributions **NH**: conceptualization (lead), data curation (lead), formal analysis (lead), investigation (lead), methodology (lead), software (lead), visualization (lead), writing – original draft (lead); **JLO**: conceptualization (supporting), data curation (supporting), investigation (supporting), software (supporting), supervision (supporting), validation (supporting), visualization (supporting), writing – review & editing (supporting); **MJM**: conceptualization (supporting), investigation (supporting), methodology (supporting), supervision (supporting), validation (supporting); **AB**: conceptualization (supporting), investigation (supporting), supervision (supporting), validation (supporting), visualization (supporting), writing – review & editing (supporting); **ES**: investigation (supporting), supervision (supporting), validation (supporting), visualization (supporting), writing – review & editing (supporting); **AS**: conceptualization (supporting), investigation (supporting), supervision (supporting), validation (supporting), visualization (supporting), writing – review & editing (supporting).

Funding This publication has been produced with funding from the Research Council of Norway [grant number 257579 (NCCS)]. Stakeholders from research, industry, vendors, and associated partners provided part of the funding.

Competing interests The authors declare that they have no known competing financial interests or personal relationships that could have appeared to influence the work reported in this paper.

Data availability The data that support the findings of this study are available from Gassnova SF, the Norwegian Petroleum Directorate and the Northern Lights JV DA but restrictions apply to the availability of these data, which were used under licence for the current study and so are not publicly available. Data are, however, available from the authors upon reasonable request and with permission of Gassnova SF, the Norwegian Petroleum Directorate and the Northern Lights JV DA.

Appendix A

A complete list of the faults modelled in this study are shown here with maximum throw and trace lengths measured in the Top Cook Formation (i.e. top secondary storage unit) horizon surface. The locations of faults are shown in Figure 5b. Stars indicate that the fault does not offset the top secondary storage unit. In addition, upsection, downsection, strike and dip attributes are added.

Fault	Maximum throw (m)	Trace length (m)	Entire trace length imaged within data limits?	Upsection extent	Downsection extent	Strike	Dip
Svartalv 1	370	6350	No	LC	B	SW	NW
Svartalv 2	300	12 000	Yes	P	B	South/SW	West/NW
Svartalv 2.1	92	2500	Yes	MJ	B	SW	NW
Tusse	940	165 000	No	N	B	South	West
F1	33	4083	Yes	LC	UT	North	East
F2	54	6641	Yes	UJ	PT	SE	SW
F3	65	6700	Yes	LC	PT	NW	NE
F4	48	8800	Yes	LC	PT	NW	NE

(continued)

Continued

Fault	Maximum throw (m)	Trace length (m)	Entire trace length imaged within data limits?	Upsection extent	Downsection extent	Strike	Dip
F5	29	8000	Yes	UJ	UT	NW	NE
F6	25	6000	Yes	LC	UT	NW	NE
F7	26	3100	Yes	UJ	UT	NW	NE
F8	13	2096	Yes	UJ	UT	North	East
F9	17	5739	Yes	UJ	UT	North	East
F10	43	7743	Yes	UJ	B	South	West
F11	76	5619	Yes	UJ	B	South	West
F12	115	4257	Yes	UJ	PT	SW	NW
F13	27	2600	Yes	UJ	UT	North	East
F14	44	6850	Yes	UJ	UT	NW	NE
F15	50	2635	Yes	LC	UT	North	East
F16	13	1064	Yes	MJ	UT	North	East
F17	37	5893	No	LC	UT	NW	NE
F18	30	3800	No	LC	UT	NW	NE
F19	21	1593	Yes	UJ	UT	North	East
F20	10	1496	Yes	UJ	LJ	North	East
F21	23	4808	No	UJ	LJ	NW	NE
F22	26	2878	Yes	UJ	LJ	North	East
F23	46	4220	Yes	UJ	UT	North	East
F24	29	2559	Yes	UJ	LJ	North	East
F25	16	2153	Yes	UJ	UT	North	East
F26	10	1868	Yes	UJ	UT	North	East
F27	32	2310	Yes	UJ	LJ	North	East
F28	13	2146	Yes	UJ	UT	NW	SE
F29	22	9	Yes	UJ	PT	North	East
F30	25	3299	Yes	UJ	UT	NW	SE
F31	30	4110	Yes	UJ	UT	NE	SE
F32	288	4300	Yes	LC	UT	NE	SE
F33	130	5249	Yes	UJ	UT	North	East
F34	25	1422	Yes	MJ	UT	North	East
F35	196	3008	Yes	UJ	UT	North	East
F36	18	632	Yes	UJ	UT	North	East
F37	19	4160	Yes	UJ	MJ	NW	East
F38	0*	0*	Yes	UJ	LJ	NW	NE
F39	80	1000	Yes	UJ	LJ	NW	NE
F40	13	596	Yes	UJ	LJ	NW	NE
F41	136	4416	Yes	UJ	PT	North	East
F42	20	6930	Yes	MJ	LJ	North	East
F43	26	8577	Yes	MJ	UT	South	West
F44	6	2758	Yes	MJ	LJ	South	West
F45	25	8083	Yes	MJ	UT	South	West
F46	35	6810	Yes	UJ	UT	SE	SW
F47	36	2975	Yes	UJ	UT	South	West
F48	33	2975	Yes	UJ	UT	SE	SW
F49	41	3846	Yes	UJ	UT	South	West
F50	31	2842	Yes	UJ	UT	SE	SW
F51	5	3408	Yes	UJ	UT	SE	SW
F52	31	2747	Yes	UJ	UT	SE	SW
F53	48	7757	Yes	UJ	UT	SE	SW
F54	26	515	Yes	UJ	UT	South	West
F55	20	4080	No	UJ	UT	SE	SW
F56	7	890	No	UJ	UT	SE	SW
F57	50	370	Yes	MJ	UT	SE	SW
F58	50	1560	No	UJ	UT	SE	SW
F59	13	540	No	UJ	UT	SE	SW
F60	40	1450	No	UJ	UT	SE	SW
F61	39	935	No	UJ	UT	SE	SW
F62	26	656	Yes	MJ	UT	West	East
F63	55	3124	Yes	UJ	PT	North	East

Abbreviations: LC, Lower Cretaceous; P, Paleogene; MJ, Middle Jurassic; N, Neogene; UJ, Upper Jurassic; UT, Upper Triassic; PT, Permian–Triassic; B, basement–cover contact.
*Does not intersect the Top Cook Formation.

Appendix B

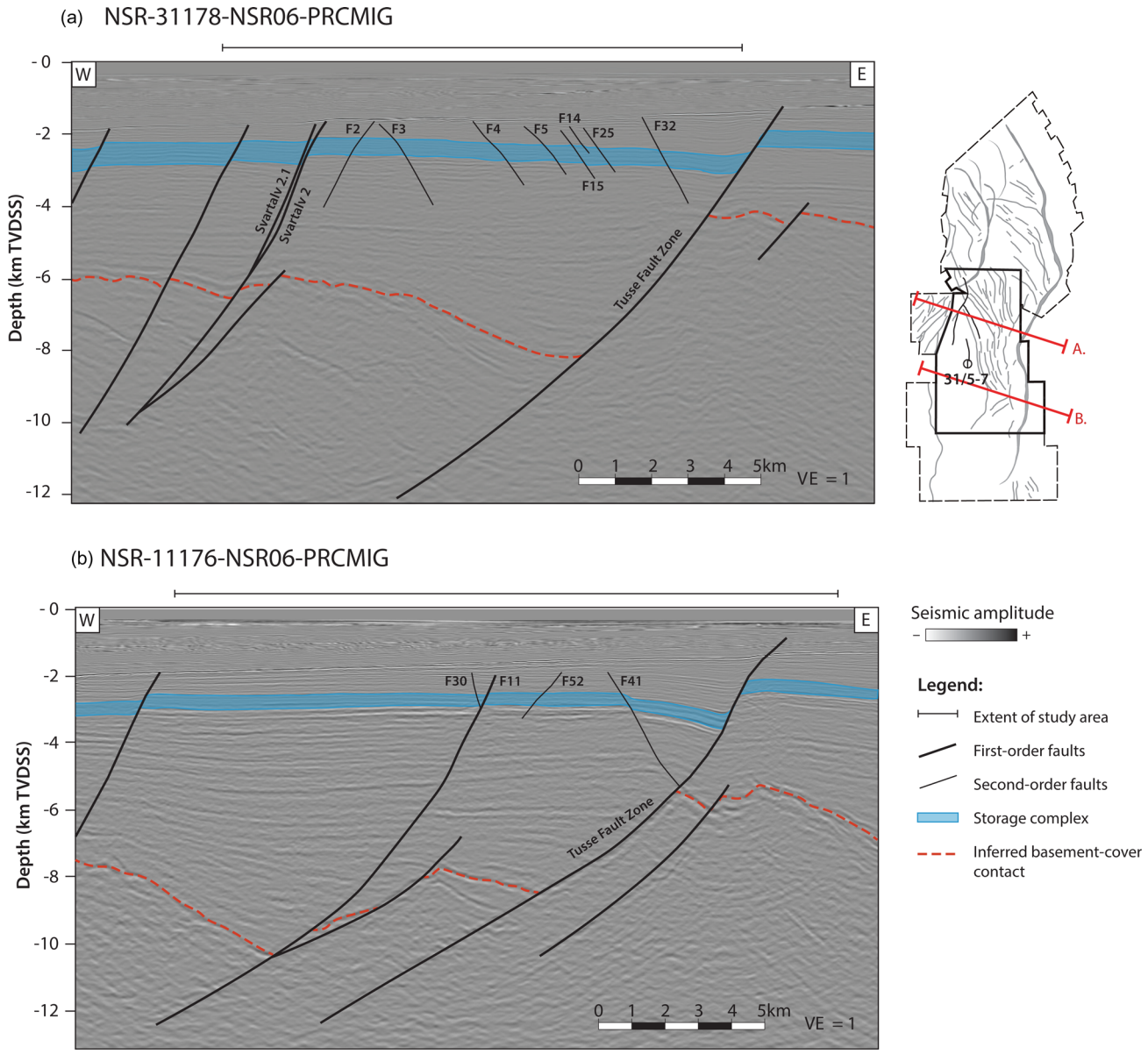

Fig. B1. Sections of regional depth-converted 2D seismic lines intersecting the study area showing the vertical extent and geometry of first- and second-order faults: (**a**) line NSR-31178-NSR06-PRCMIG and (**b**) NSR-11176-NSR06-PRCMIG. The intended storage complex within Aurora is highlighted in blue and the inferred basement–cover contact with a dashed red line. The inset map shows the location of the 2D lines. See Figure 5b for the locations of the interpreted faults within the study area.

References

Allan, U.S. 1989. Model for hydrocarbon migration and entrapment within faulted structures. *AAPG Bulletin*, **73**, 803–811.

Andersen, T.B. and Jamtveit, B. 1990. Uplift of deep crust during orogenic extensional collapse: a model based on field studies in the Sogn-Sunnfjord Region of western Norway. *Tectonics*, **9**, 1097–1111, https://doi.org/10.1029/TC009i005p01097

Anell, I., Thybo, H. and Rasmussen, E. 2012. A synthesis of Cenozoic sedimentation in the North Sea. *Basin Research*, **24**, 154–179, https://doi.org/10.1111/j.1365-2117.2011.00517.x

Arts, R., Chadwick, A., Eiken, O., Thibeau, S. and Nooner, S. 2008. Ten years' experience of monitoring CO_2 injection in the Utsira Sand at Sleipner, offshore Norway. *First Break*, **26**, 65–72, https://doi.org/10.3997/1365-2397.26.1115.27807

Badley, M., Price, J., Dahl, C.R. and Agdestein, T. 1988. The structural evolution of the northern Viking Graben and its bearing upon extensional modes of basin formation. *Journal of the Geological Society, London*, **145**, 455–472, https://doi.org/10.1144/gsjgs.145.3.0455

Bartholomew, I.D., Peters, J.M. and Powell, C.M. 1993. Regional structural evolution of the North Sea: oblique slip and the reactivation of basement lineaments. *Geological Society, London, Petroleum Geology Conference Series*, **4**, 1109–1122, https://doi.org/10.1144/0041109

Bell, R.E., Jackson, C.A.L., Whipp, P.S. and Clements, B. 2014. Strain migration during multiphase extension: observations from the northern North Sea. *Tectonics*, **33**, 1936–1963, https://doi.org/10.1002/2014TC003551

Benson, S.M. and Cole, D.R. 2008. CO_2 sequestration in deep sedimentary formations. *Elements*, **4**, 325–331, https://doi.org/10.2113/gselements.4.5.325

Bjørlykke, K. 1993. Fluid flow in sedimentary basins. *Sedimentary Geology*, **86**, 137–158, https://doi.org/10.1016/0037-0738(93)90137-T

Braathen, A. and Erambert, M. 2014. Structural and metamorphic history of the Engebøfjellet Eclogite and the exhumation of the Western Gneiss Region, Norway. *Norwegian Journal of Geology/Norsk Geologisk Tidsskrift*, **94**, 53–76.

Braathen, A., Nordgulen, Ø., Osmundsen, P.-T., Andersen, T.B., Solli, A. and Roberts, D. 2000. Devonian, orogen-parallel, opposed extension in the Central Norwegian Caledonides. *Geology*, **28**, 615–618, https://doi.org/10.1130/0091-7613(2000)28%3C615:DOOEIT%3E2.0.CO;2

Braathen, A., Midtkandal, I., Mulrooney, M.J., Appleyard, T.R., Haile, B.G. and van Yperen, A.E. 2018*a*. Growth-faults from delta collapse – structural and sedimentological investigation of the Last Chance delta, Ferron Sandstone, Utah. *Basin Research*, **30**, 688–707, https://doi.org/10.1111/bre.12271

Braathen, A., Osmundsen, P.T., Maher, H. and Ganerød, M. 2018*b*. The Keisarhjelmen detachment records Silurian–Devonian extensional collapse in northern Svalbard. *Terra Nova*, **30**, 34–39, https://doi.org/10.1111/ter.12305

Brekke, H., Sjulstad, H., Magnus, C. and Williams, R. 2001. Sedimentary environments offshore Norway–Palaeozoic to recent. *Norwegian Petroleum Society Special Publications*, **10**, 7–37, https://doi.org/10.1016/S0928-8937(01)80006-0

Bretan, P. 2017. Trap Analysis: an automated approach for deriving column height predictions in fault-bounded traps. *Petroleum Geoscience*, **23**, 56–69, https://doi.org/10.1144/10.44petgeo2016-022

Bretan, P., Yielding, G. and Jones, H. 2003. Using calibrated shale gouge ratio to estimate hydrocarbon column heights. *AAPG Bulletin*, **87**, 397–413, https://doi.org/10.1306/08010201128

Bretan, P., Yielding, G., Mathiassen, O.M. and Thorsnes, T. 2011. Fault-seal analysis for CO_2 storage: an example from the Troll area, Norwegian Continental Shelf. *Petroleum Geoscience*, **17**, 181–192, https://doi.org/10.1144/1354-079310-025

Cartwright, J. and Mansfield, C. 1998. Lateral displacement variation and lateral tip geometry of normal fault in the Canyonlands National Park. *Journal of Structural Geology*, **20**, 3–19, https://doi.org/10.1016/S0191-8141(97)00079-5

Cartwright, J., Bouroullec, R., James, D. and Johnson, H. 1998. Polycyclic motion history of some Gulf Coast growth faults from high-resolution displacement analysis. *Geology*, **26**, 819–822, https://doi.org/10.1130/0091-7613(1998)026%3C0819:PMHOSG%3E2.3.CO;2

Childs, C., Walsh, J.J. and Watterson, J. 1997. Complexity in fault zone structure and implications for fault seal prediction. *Norwegian Petroleum Society Special Publications*, **7**, 61–72, https://doi.org/10.1016/S0928-8937(97)80007-0

Childs, C., Sylta, Ø., Moriya, S., Morewood, N., Manzocchi, T., Walsh, J.J. and Hermanssen, D. 2009. Calibrating fault seal using a hydrocarbon migration model of the Oseberg Syd area, Viking Graben. *Marine and Petroleum Geology*, **26**, 764–774, https://doi.org/10.1016/j.marpetgeo.2008.05.004

Clausen, J., Gabrielsen, R., Reksnes, P. and Nysaether, E. 1999. Development of intraformational (Oligocene–Miocene) faults in the northern North Sea: influence of remote stresses and doming of Fennoscandia. *Journal of Structural Geology*, **21**, 1457–1475, https://doi.org/10.1016/S0191-8141(99)00083-8

Corfu, F., Andersen, T. and Gasser, D. 2014. The Scandinavian Caledonides: main features, conceptual advances and critical questions. *Geological Society, London, Special Publications*, **390**, 9–43, https://doi.org/10.1144/SP390.25

Coward, M. 1990. The Precambrian, Caledonian and Variscan framework to NW Europe. *Geological Society, London, Special Publications*, **55**, 1–34, https://doi.org/10.1144/GSL.SP.1990.055.01.01

Coward, M., Dewey, J., Hempton, M. and Holroyd, J. 2003. Tectonic evolution. *In:* Evans, D., Graham, C., Armour, A. and Bathurst, P. (eds) *The Millennium Atlas: Petroleum Geology of the Central and Northern North Sea*. Geological Society, London, 26–65.

Cowie, P.A., Underhill, J.R., Behn, M.D., Lin, J. and Gill, C.E. 2005. Spatio-temporal evolution of strain accumulation derived from multi-scale observations of Late Jurassic rifting in the northern North Sea: a critical test of models for lithospheric extension. *Earth and Planetary Science Letters*, **234**, 401–419, https://doi.org/10.1016/j.epsl.2005.01.039

Crameri, F. 2021. *Scientific Colour Maps (v.7.0.0)*. Zenodo, https://zenodo.org/record/5501399#.YdLCgWjMKUk [last accessed 3 January 2022].

Cunningham, J., Cardozo, N., Townsend, C. and Callow, R. 2020. The Impact of seismic interpretation methods on the analysis of faults: a case study from the Snøhvit field, Barents Sea. *Solid Earth Discussions*, **12**, 1–48, https://doi.org/10.5194/se-12-741-2021

Davies, R.J., Turner, J. and Underhill, J.R. 2001. Sequential dip-slip fault movement during rifting: a new model for the evolution of the Jurassic trilete North Sea rift system. *Petroleum Geoscience*, **7**, 371–388, https://doi.org/10.1144/petgeo.7.4.371

Deegan, C. and Scull, B. 1977. *A Standard Lithostratigraphic Nomenclature for the Central and the Northern North Sea*. *Norwegian Petroleum Directorate Bulletin*, **1**.

Deng, C., Fossen, H., Gawthorpe, R.L., Rotevatn, A., Jackson, C.A. and FazliKhani, H. 2017. Influence of fault reactivation during multiphase rifting: the Oseberg area, northern North Sea rift. *Marine and Petroleum Geology*, **86**, 1252–1272, https://doi.org/10.1016/j.marpetgeo.2017.07.025

Downey, M.W. 1984. Evaluating seals for hydrocarbon accumulations. *AAPG Bulletin*, **68**, 1752–1763, https://doi.org/10.1306/AD461994-16F7-11D7-8645000102C1865D

Downey, M.W. 1994. Hydrocarbon seal rocks. *AAPG Memoirs*, **60**, 159–164, https://doi.org/10.1306/M60585C8

Dreyer, T., Whitaker, M., Dexter, J., Flesche, H. and Larsen, E. 2005. From spit system to tide-dominated delta: integrated reservoir model of the Upper Jurassic Sognefjord Formation on the Troll West Field. *Geological Society, London, Petroleum Geology Conference Series*, **6**, 423–448, https://doi.org/10.1144/0060423

Duffy, O.B., Bell, R.E., Jackson, C.A.-L., Gawthorpe, R.L. and Whipp, P.S. 2015. Fault growth and interactions in a multiphase rift fault network: Horda Platform, Norwegian North Sea. *Journal of Structural Geology*, **80**, 99–119, https://doi.org/10.1016/j.jsg.2015.08.015

Eidvin, T. and Rundberg, Y. 2007. Post-Eocene strata of the southern Viking Graben, northern North Sea; integrated biostratigraphic, strontium isotopic and lithostratigraphic study. *Norwegian Journal of Geology/Norsk Geologisk Tidsskrift*, **87**, 391–450.

Eidvin, T., Riis, F. and Rasmussen, E.S. 2014. Oligocene to Lower Pliocene deposits of the Norwegian continental shelf, Norwegian Sea, Svalbard, Denmark and their relation to the uplift of Fennoscandia: a synthesis. *Marine and Petroleum Geology*, **56**, 184–221, https://doi.org/10.1016/j.marpetgeo.2014.04.006

Equinor ASA 2021. *Northern Lights Project Concept report*. Equinor ASA, Stavanger, Norway, Document RE-PM673-00001. https://norlights.com/wp-content/uploads/2021/03/Northern-Lights-Project-Concept-report.pdf [last accessed 29 September 2022].

Equinor ASA 2022. Sharing data from Northern Lights well. Equinor ASA, Stavanger, Norway, https://www.equinor.com/en/news/20201019-sharing-data-northern-lights.html [last accessed 21 February 2022].

Færseth, R. 1996. Interaction of Permo-Triassic and Jurassic extensional fault-blocks during the development of the northern North Sea. *Journal of Geological Society, London*, **153**, 931–944, https://doi.org/10.1144/gsjgs.153.6.0931

Færseth, R. and Ravnås, R. 1998. Evolution of the Oseberg fault-block in context of the northern North Sea structural framework. *Marine and Petroleum Geology*, **15**, 467–490, https://doi.org/10.1016/S0264-8172(97)00046-9

Færseth, R.B., Gabrielsen, R.H. and Hurich, C.A. 1995. Influence of basement in structuring of the North Sea basin, offshore southwest Norway. *Norwegian Journal of Geology/Norsk Geologisk Tidsskrift*, **75**, 105–119.

Færseth, R.B., Johnsen, E. and Sperrevik, S. 2007. Methodology for risking fault seal capacity: implications of fault zone architecture. *AAPG Bulletin*, **91**, 1231–1246, https://doi.org/10.1306/03080706051

Faleide, J.I., Kyrkjebo, R., Kjennerud, T., Gabrielsen, R.H., Jordt, H., Fanavoll, S. and Bjerke, M.D. 2002. Tectonic impact on sedimentary processes during Cenozoic evolution of the northern North Sea and surrounding areas. *Geological Society, London, Special Publications*, **196**, 235–270, https://doi.org/10.1144/GSL.SP.2002.196.01.14

Faleide, J.I., Bjørlykke, K. and Gabrielsen, R.H. 2010. Geology of the Norwegian continental shelf. *In:* Bjørlykke, K. (ed.) *Petroleum Geoscience*. Springer, Heidelberg, 603–637.

Fazlikhani, H., Fossen, H., Gawthorpe, R., Faleide, J.I. and Bell, R.E. 2017. Basement structure and its influence on the structural configuration of the northern North Sea rift. *Tectonics*, **36**, 1151–1177, https://doi.org/10.1002/2017TC004514

Fazlikhani, H., Aagotnes, S.S. *et al.* 2021. Strain migration during multiphase extension, Stord Basin, northern North Sea rift. *Basin Research*, **33**, 1474–1496, https://doi.org/10.1111/bre.12522

Fisher, Q. and Knipe, R.J. 1998. Fault sealing processes in siliciclastic sediments. *Geological Society, London, Special Publications*, **147**, 117–134, https://doi.org/10.1144/GSL.SP.1998.147.01.08

Fisher, Q. and Knipe, R. 2001. The permeability of faults within siliciclastic petroleum reservoirs of the North Sea and Norwegian Continental Shelf. *Marine and Petroleum Geology*, **18**, 1063–1081, https://doi.org/10.1016/S0264-8172(01)00042-3

Fossen, H. 2010. Extensional tectonics in the North Atlantic Caledonides: a regional view. *Geological Society, London, Special Publications*, **335**, 767–793, https://doi.org/10.1144/SP335.31

Fossen, H. and Rotevatn, A. 2016. Fault linkage and relay structures in extensional settings – a review. *Earth-Science Reviews*, **154**, 14–28, https://doi.org/10.1016/j.earscirev.2015.11.014

Fossen, H., Schultz, R.A., Shipton, Z.K. and Mair, K. 2007. Deformation bands in sandstone: a review. *Journal of the Geological Society, London*, **164**, 755–769, https://doi.org/10.1144/0016-76492006-036

Freeman, B., Yielding, G., Needham, D.T. and Badley, M.E. 1998. Fault seal prediction: the gouge ratio method. *Geological Society, London, Special Publications*, **127**, 19–25, https://doi.org/10.1144/GSL.SP.1998.127.01.03

Fristad, T., Groth, A., Yielding, G. and Freeman, B. 1997. Quantitative fault seal prediction: a case study from Oseberg Syd. *Norwegian Petroleum Society Special Publications*, **7**, 107–124, https://doi.org/10.1016/S0928-8937(97)80010-0

Furre, A.-K., Meneguolo, R., Ringrose, P. and Kassold, S. 2019. Building confidence in CCS: from Sleipner to the Northern Lights project. *First Break*, **37**, 81–87, https://doi.org/10.3997/1365-2397.n0038

Furre, A.-K., Meneguolo, R., Pinturier, L. and Bakke, K. 2020. Planning deep subsurface CO_2 storage monitoring for the Norwegian full-scale CCS project. *First Break*, **38**, 55–60, https://doi.org/10.3997/1365-2397.fb2020074

Gabrielsen, R.H. 1984. Long-lived fault zones and their influence on the tectonic development of the southwestern Barents Sea. *Journal of the Geological Society, London*, **141**, 651–662, https://doi.org/10.1144/gsjgs.141.4.0651

Gabrielsen, R.H., Kyrkjebø, R., Faleide, J.I., Fjeldskaar, W. and Kjennerud, T. 2001. The Cretaceous post-rift basin configuration of the northern North Sea. *Petroleum Geoscience*, **7**, 137–154, https://doi.org/10.1144/petgeo.7.2.137

Gassnova 2012. *Geological Storage of CO_2 from Mongstad*. Interim Report Johansen Formation, Document TL02-GTL-Z-RA-0001.

Gassnova 2020. *Demonstrasjon av fullskala CO2-håndtering - Rapport for avsluttende forprosjekt*. Gassnova Full-Chain Report. Document 17/35-1, https://gassnova.no/app/uploads/sites/6/2020/10/Gassnovas-helkjederapport-redacted-version-som-publisert.pdf [last accessed 29 September 2022].

Gee, D.G., Fossen, H., Henriksen, N. and Higgins, A.K. 2008. From the early Paleozoic platforms of Baltica and Laurentia to the Caledonide Orogen of Scandinavia and Greenland. *Episodes*, **31**, 44–51, https://doi.org/10.18814/epiiugs/2008/v31i1/007

Glennie, K. 1990. Outline of North Sea history and structural framework. *In:* Glennie, K. (ed.) *Introduction to the Petroleum Geology of the North Sea*. Blackwell Scientific, Oxford, UK, 34–77.

Helland-Hansen, W., Ashton, M., Lømo, L. and Steel, R. 1992. Advance and retreat of the Brent delta: recent contributions to the depositional model. *Geological Society, London, Special Publications*, **61**, 109–127, https://doi.org/10.1144/GSL.SP.1992.061.01.07

Henza, A.A., Withjack, M.O. and Schlische, R.W. 2010. Normal-fault development during two phases of non-coaxial extension: an experimental study. *Journal of Structural Geology*, **32**, 1656–1667, https://doi.org/10.1016/j.jsg.2009.07.007

Hongxing, G. and Anderson, J.K. 2007. Fault throw profile and kinematics of normal faults: conceptual models and geologic examples. *Geological Journal of China Universities*, **13**, 75–88.

Husmo, T., Hamar, G., Høiland, O., Johannessen, E., Rømuld, A., Spencer, A. and Titterton, R. 2002. Lower and Middle Jurassic. *In:* Evans, D., Graham, C., Armour, A. and Bathurst, P. (eds) *The Millennium Atlas: Petroleum Geology of the Central and Northern North Sea*. Geological Society, London, 129–155.

IEA 2021. *Net Zero by 2050: A Roadmap for the Global Energy Section*. Flagship Report. International Energy Agency (IEA), Paris.

Iglauer, S., Al-Yaseri, A.Z., Rezaee, R. and Lebedev, M. 2015. CO_2 wettability of caprocks: implications for structural storage capacity and containment security. *Geophysical Research Letters*, **42**, 9279–9284, https://doi.org/10.1002/2015GL065787

IPCC 2018. *Global Warming of 1.5°C*. Intergovernmental Panel on Climate Change Special Report. Intergovernmental Panel on Climate Change (IPCC), Geneva, Switzerland.

Jackson, C.A.-L. and Rotevatn, A. 2013. 3D seismic analysis of the structure and evolution of a salt-influenced normal fault zone: a test of competing fault growth models. *Journal of Structural Geology*, **54**, 215–234, https://doi.org/10.1016/j.jsg.2013.06.012

Jarsve, E.M., Maast, T.E., Gabrielsen, R.H., Faleide, J.I., Nystuen, J.P. and Sassier, C. 2014. Seismic stratigraphic subdivision of the Triassic succession in the Central North Sea; integrating seismic reflection and well data. *Journal of the Geological Society, London*, **171**, 353–374, https://doi.org/10.1144/jgs2013-056

Jones, R.M. and Hillis, R.R. 2003. An integrated, quantitative approach to assessing fault-seal risk. *AAPG Bulletin*, **87**, 507–524, https://doi.org/10.1306/10100201135

Karolytė, R., Johnson, G., Yielding, G. and Gilfillan, S.M. 2020. Fault seal modelling – the influence of fluid properties on fault sealing capacity in hydrocarbon and CO_2 systems. *Petroleum Geoscience*, **26**, 481–497, https://doi.org/10.1144/petgeo2019-126

Knipe, R.J. 1992. Faulting processes and fault seal. *Norwegian Petroleum Society Special Publications*, **1**, 325–342, https://doi.org/10.1016/B978-0-444-88607-1.50027-9

Knipe, R.J. 1997. Juxtaposition and seal diagrams to help analyze fault seals in hydrocarbon reservoirs. *AAPG Bulletin*, **81**, 187–195, https://doi.org/10.1306/522B42DF-1727-11D7-8645000102C1865D

Knott, S.D. 1993. Fault seal analysis in the North Sea. *AAPG Bulletin*, **77**, 778–792, https://doi.org/10.1306/BDFF8D58-1718-11D7-8645000102C1865D

Kyrkjebø, R., Gabrielsen, R. and Faleide, J. 2004. Unconformities related to the Jurassic–Cretaceous synrift–post-rift transition of the northern North Sea. *Journal of the Geological Society, London*, **161**, 1–17, https://doi.org/10.1144/0016-764903-051

Lervik, K. 2006. Triassic lithostratigraphy of the northern North Sea Basin. *Norwegian Journal of Geology/Norsk Geologisk Tidsskrift*, **86**, 93–117.

Lindsay, N., Murphy, F., Walsh, J. and Watterson, J. 1993. Outcrop studies of shale smears on fault surfaces. *In:* Flint, S. and Bryant, I. (eds) *The Geological Modelling of Hydrocarbon Reservoirs and Outcrop Analogues*. Blackwell Scientific, Oxford, UK, 113–123, 34–77.

Lyon, P., Boult, P., Mitchell, A. and Hillis, R. 2004. Improving fault geometry interpretation through 'pseudo-depth' conversion of seismic data in the Penola Trough, Otway Basin. *In:* Boult, P., Johns, D. and Lang, S. (eds) Eastern Australian Basin Symposium II. Petroleum Exploration Society of Australia Special Publications, 395–706.

Lyon, P.J., Boult, P.J., Hillis, R.R. and Mildren, S.D. 2005. Sealing by shale gouge and subsequent seal breach by reactivation: a case study of the Zema Prospect, Otway Basin. *AAPG Hedberg Series*, **2**, 179–197, https://doi.org/10.1306/1060764H23169

Manzocchi, T., Childs, C. and Walsh, J. 2010. Faults and fault properties in hydrocarbon flow models. *Geofluids*, **10**, 94–113, https://doi.org/10.1111/j.1468-8123.2010.00283.x

Marjanac, T. and Steel, R.J. 1997. Dunlin Group sequence stratigraphy in the northern North Sea: a model for Cook Sandstone deposition. *AAPG Bulletin*, **81**, 276–292, https://doi.org/10.1306/522B4307-1727-11D7-8645000102C1865D

Meneguolo, R., Sundal, A., Martinius, A.W., Veselovsky, Z., Cullum, A. and Milovanova, E. 2022. Impact of the lower Jurassic Dunlin Group depositional elements on the Aurora CO_2 storage site, EL001, northern North Sea, Norway. *International Journal of Greenhouse Gas Control*, **119**, 103723, https://doi.org/10.1016/j.ijggc.2022.103723

Michie, E.A.H., Mulrooney, M.J. and Braathen, A. 2021. Fault interpretation uncertainties using seismic data, and the effects on fault seal analysis: a case study from the Horda platform, with implications for CO_2 storage. *Solid Earth*, **12**, 1259–1286, https://doi.org/10.5194/se-12-1259-2021

Miocic, J., Johnson, G. and Bond, C.E. 2019. Uncertainty in fault seal parameters: implications for CO_2 column height retention and storage capacity in geological CO_2 storage projects. *Solid Earth*, **10**, 951–967, https://doi.org/10.5194/se-10-951-2019

Mulrooney, M.J., Osmond, J.L., Skurtveit, E., Faleide, J.I. and Braathen, A. 2020. Structural analysis of the Smeaheia fault block, a potential CO_2 storage site, northern Horda Platform, North Sea. *Marine and Petroleum Geology*, **121**, 104598, https://doi.org/10.1016/j.marpetgeo.2020.104598

Nedberg, H.C. 2022. *Fault Reactivation Potential of the Aurora Area, Northern North Sea: Implications for Successful Storage of CO_2*. Master's dissertation, University of Oslo, Oslo, Norway.

NMPE 2020. *Longship – Carbon Capture and Storage*. Meld. St. 33 (2019–2020) Report to the Storting (White Paper). Norwegian Ministry of Petroleum and Energy (NMPE), Oslo.

Norton, M., Coney, P. and Davis, G. 1986. Collapse of the Caledonian orogen and the Old Red Sandstone. *Nature*, **323**, 147–149, https://doi.org/10.1038/323147a0

Nottvedt, A., Gabrielsen, R. and Steel, R. 1995. Tectonostratigraphy and sedimentary architecture of rift basins, with reference to the northern North Sea. *Marine and Petroleum Geology*, **12**, 881–901, https://doi.org/10.1016/0264-8172(95)98853-W

NPD 2014. *Lithostratigraphic Chart – Norwegian North Sea*. Norwegian Petroleum Directorate (NPD), Stavanger, Norway.

NPD FactMaps 2020. *Norwegian Petroleum Directorate FactMaps*. Norwegian Petroleum Directorate (NPD), Stavanger, Norway, https://factmaps.npd.no/factmaps/3_0/?run=FieldByNPDID&NPDID=46437 [last accessed 23 April 2020].

NPD FactPages 2020. *Norwegian Petroleum Directorate FactPages*. Norwegian Petroleum Directorate (NPD), Stavanger, Norway, https://factpages.npd.no/ [last accessed 8 August 2020].

Odinsen, T., Christiansson, P., Gabrielsen, R.H., Faleide, J.I. and Berge, A.M. 2000*a*. The geometries and deep structure of the northern North Sea rift. *Geological Society, London, Special Publications*, **167**, 41–57, https://doi.org/10.1144/GSL.SP.2000.167.01.03

Odinsen, T., Reemst, P., Van Der Beek, P., Faleide, J.I. and Gabrielsen, R.H. 2000*b*. Permo-Triassic and Jurassic extension in the northern North Sea: results from tectonostratigraphic forward modelling. *Geological Society, London, Special Publications*, **167**, 83–103, https://doi.org/10.1144/GSL.SP.2000.167.01.05

Osmond, J.L. and Meckel, T.A. 2020. Enhancing trap and fault seal analyses by integrating observations from HR3D seismic data with well logs and conventional 3D seismic data, Texas inner shelf. *Geological Society, London, Special Publications*, **496**, 253–279, https://doi.org/10.1144/SP496-2018-142

Osmond, J.L., Mulrooney, M.J., Holden, N., Skurtveit, E., Faleide, J.I. and Braathen, A. 2022. Structural traps and seals for expanding CO_2 storage in the northern Horda Platform, North Sea. *AAPG Bulletin*, **96**, https://doi.org/10.1306/03222221110

Osmundsen, P.T. and Andersen, T.B. 2001. The middle Devonian basins of western Norway: sedimentary response to large-scale transtensional tectonics? *Tectonophysics*, **332**, 51–68, https://doi.org/10.1016/S0040-1951(00)00249-3

Osmundsen, P.T., Bakke, B., Svendby, A.K. and Andersen, T.B. 2000. Architecture of the Middle Devonian Kvamshesten Group, western Norway: sedimentary response to deformation above a ramp-flat extensional fault. *Geological Society, London, Special Publications*, **180**, 503–535, https://doi.org/10.1144/GSL.SP.2000.180.01.27

Osmundsen, P.T., Eide, E. *et al.* 2006. Kinematics of the Høybakken detachment zone and the Møre–Trøndelag Fault Complex, central Norway. *Journal of the Geological Society, London*, **163**, 303–318, https://doi.org/10.1144/0016-764904-129

Pei, Y., Paton, D., Knipe, R. and Wu, K. 2015. A review of fault sealing behaviour and its evaluation in siliciclastic rocks. *Earth-Science Reviews*, **150**, 121–138, https://doi.org/10.1016/j.earscirev.2015.07.011

Phillips, T.B., Fazlikhani, H. *et al.* 2019. The Influence of structural inheritance and multiphase extension on rift development, the Northern North Sea. *Tectonics*, **38**, 4099–4126, https://doi.org/10.1029/2019tc005756

Rahman, M.J., Choi, J.C., Fawad, M. and Mondol, N.H. 2021. Probabilistic analysis of Vette fault stability in potential CO_2 storage site Smeaheia, offshore Norway. *International Journal of Greenhouse Gas Control*, **108**, 103315, https://doi.org/10.1016/j.ijggc.2021.103315

Rahman, M.J., Fawad, M., Jahren, J. and Mondol, N.H. 2022*a*. Influence of depositional and diagenetic processes on Caprock properties of CO_2 storage sites in the Northern North Sea, offshore Norway. *Geosciences*, **12**, 181, https://doi.org/10.3390/geosciences12050181

Rahman, M.J., Fawad, M., Jahren, J. and Mondol, N.H. 2022*b*. Top seal assessment of Drake Formation shales for CO_2 storage in the Horda Platform area, offshore Norway. *International Journal of Greenhouse Gas Control*, **119**, 103700, https://doi.org/10.1016/j.ijggc.2022.103700

Randen, T. and Sønneland, L. 2005. Atlas of 3D seismic attributes. *In:* Iske, A. and Sønneland, L. (eds) *Mathematical Methods and Modelling in Hydrocarbon Exploration and Production*. Mathematics in Industry, **7**. Springer, Berlin, 23–46, https://doi.org/10.1007/3-540-26493-0_2

Ravnås, R., Nøttvedt, A., Steel, R. and Windelstad, J. 2000. Syn-rift sedimentary architectures in the Northern North Sea. *Geological Society, London, Special Publications*, **167**, 133–177, https://doi.org/10.1144/GSL.SP.2000.167.01.07

Roberts, A., Yielding, G., Kusznir, N., Walker, I. and Dorn-Lopez, D. 1993. Mesozoic extension in the North Sea: constraints from flexural backstripping, forward modelling and fault populations. *Geological Society, London, Petroleum Geology Conference Series*, **4**, 1123–1136, https://doi.org/10.1144/0041123

Roberts, A., Yielding, G., Kusznir, N., Walker, I. and Dorn-Lopez, D. 1995. Quantitative analysis of Triassic extension in the northern Viking Graben. *Journal of the Geological Society, London*, **152**, 15–26, https://doi.org/10.1144/gsjgs.152.1.0015

Skurtveit, E., Choi, J.C., Osmond, J., Mulrooney, M. and Braathen, A. 2018. 3D fault integrity screening for Smeaheia CO_2 injection site. *14th Greenhouse Gas Control Technologies Conference Melbourne 21–26 October 2018 (GHGT-14)*, https://doi.org/10.2139/ssrn.3366335

Smith, D.A. 1966. Theoretical considerations of sealing and non-sealing faults. *AAPG Bulletin*, **50**, 363–374, https://doi.org/10.1306/5D25B48F-16C1-11D7-8645000102C1865D

Sneider, J.S., de Clarens, P. and Vail, P.R. 1995. Sequence stratigraphy of the Middle to Upper Jurassic, Viking Graben, North Sea. *Norwegian Petroleum Society Special Publications*, **5**, 167–197, https://doi.org/10.1016/S0928-8937(06)80068-8

Sperrevik, S., Gillespie, P.A., Fisher, Q.J., Halvorsen, T. and Knipe, R.J. 2002. Empirical estimation of fault rock properties. *Norwegian Petroleum Society Special Publications*, **11**, 109–125, https://doi.org/10.1016/S0928-8937(02)80010-8

Steel, R. 1993. Triassic–Jurassic megasequence stratigraphy in the Northern North Sea: rift to post-rift evolution. *Geological Society, London, Petroleum Geology Conference Series*, **4**, 299–315, https://doi.org/10.1144/0040299

Steel, R. and Ryseth, A. 1990. The Triassic–Early Jurassic succession in the northern North Sea: megasequence stratigraphy and intra-Triassic tectonics. *Geological Society, London, Special Publications*, **55**, 139–168, https://doi.org/10.1144/GSL.SP.1990.055.01.07

Stewart, D., Schwander, M. and Bolle, L. 1995. Jurassic depositional systems of the Horda Platform, Norwegian North Sea: practical consequences of applying sequence stratigraphic models. *Norwegian Petroleum Society Special Publications*, **5**, 291–323, https://doi.org/10.1016/S0928-8937(06)80073-1

Sturt, B.A. and Braathen, A. 2001. Deformation and metamorphism of Devonian rocks in the outer Solund area, western Norway: implications for models of Devonian deformation. *International Journal of Earth Sciences*, **90**, 270–286, https://doi.org/10.1007/s005310000131

Sundal, A., Miri, R., Ravn, T. and Aagaard, P. 2015. Modelling CO_2 migration in aquifers; considering 3D seismic property data and the effect of site-typical depositional heterogeneities. *International Journal of Greenhouse Gas Control*, **39**, 349–365, https://doi.org/10.1016/j.ijggc.2015.05.021

Sundal, A., Nystuen, J.P., Rørvik, K.-L., Dypvik, H. and Aagaard, P. 2016. The Lower Jurassic Johansen Formation, northern North Sea – Depositional model and reservoir characterization for CO_2 storage. *Marine and Petroleum Geology*, **77**, 1376–1401, https://doi.org/10.1016/j.marpetgeo.2016.01.021

Tearpock, D.J. and Bischke, R.E. 2002. *Applied Subsurface Geological Mapping with Structural Methods*. 2nd edn. Pearson Education, London.

Thompson, N., Andrews, J.S., Wu, L. and Meneguolo, R. 2022. Characterization of the in-situ stress on the Horda platform–a study from the Northern Lights Eos well. *International Journal of Greenhouse Gas Control*, **114**, 103580, https://doi.org/10.1016/j.ijggc.2022.103580

Thorsen, C.E. 1963. Age of growth faulting in southeast Louisiana. *Gulf Coast Association of Geological Societies Transactions*, **13**, 103–110.

Tillmans, F., Gawthorpe, R.L., Jackson, C.A.L. and Rotevatn, A. 2021. Syn-rift sediment gravity flow deposition on a Late Jurassic fault-terraced slope, northern North Sea. *Basin Research*, **33**, 1844–1879, https://doi.org/10.1111/bre.12538

Torp, T.A. and Gale, J. 2004. Demonstrating storage of CO_2 in geological reservoirs: The Sleipner and SACS projects. *Energy*, **29**, 1361–1369, https://doi.org/10.1016/j.energy.2004.03.104

Underhill, J.R. and Partington, M. 1993. Jurassic thermal doming and deflation in the North Sea: implications of the sequence stratigraphic evidence. *Geological Society, London, Petroleum Geology Conference Series*, **4**, 337–345, https://doi.org/10.1144/0040337

Vollset, J. and Doré, A.G. 1984. *A Revised Triassic and Jurassic Lithostratigraphic Nomenclature for the Norwegian North Sea*. Norwegian Petroleum Directorate (NPD), Stavanger, Norway.

Watts, N. 1987. Theoretical aspects of cap-rock and fault seals for single- and two-phase hydrocarbon columns. *Marine and Petroleum Geology*, **4**, 274–307, https://doi.org/10.1016/0264-8172(87)90008-0

Whipp, P., Jackson, C.L., Gawthorpe, R., Dreyer, T. and Quinn, D. 2014. Normal fault array evolution above a reactivated rift fabric; a subsurface example from the northern Horda Platform, Norwegian North Sea. *Basin Research*, **26**, 523–549, https://doi.org/10.1111/bre.12050

Wiest, J., Fossen, H. and Jacobs, J. 2020. Shear zone evolution during core complex exhumation – implications for continental detachments. *Journal of Structural Geology*, **140**, 104139, https://doi.org/10.1016/j.jsg.2020.104139

Wiest, J., Jacobs, J., Fossen, H., Ganerød, M. and Osmundsen, P. 2021. Segmentation of the Caledonian orogenic infrastructure and exhumation of the Western Gneiss Region during transtensional collapse. *Journal of the Geological Society, London*, **178**, https://doi.org/10.1144/jgs2020-199

Wu, L., Thorsen, R., Ringrose, P., Ottesen, S. and Hartvedt, K. 2021. Significance of fault seal in assessing CO_2 storage capacity and leakage risks – an example from offshore Norway. *Petroleum Geoscience*, **27**, 1–20, https://doi.org/10.1144/petgeo2020-102

Würtzen, C.L., Osmond, J.L., Faleide, J.I., Nystuen, J.P., Anell, I.M. and Midtkandal, I. 2021. Syn- to post-rift alluvial basin fill: seismic stratigraphic analysis of Permian-Triassic deposition in the Horda Platform, Norway. *Basin Research*, **34**, 883–912, https://doi.org/10.1111/bre.12644

Yielding, G. 2002. Shale gouge ratio – calibration by geohistory. *Norwegian Petroleum Society Special Publications*, **11**, 1–15, https://doi.org/10.1016/S0928-8937(02)80003-0

Yielding, G., Freeman, B. and Needham, D.T. 1997. Quantitative fault seal prediction. *AAPG Bulletin*, **81**, 897–917, https://doi.org/10.1306/522B498D-1727-11D7-8645000102C1865D

Yielding, G., Bretan, P. and Freeman, B. 2010. Fault seal calibration: a brief review. *Geological Society, London, Special Publications*, **347**, 243–255, https://doi.org/10.1144/SP347.14

Zhong, X. and Escalona, A. 2020. Evidence of rift segmentation and controls of Middle to Late Jurassic synrift deposition in the Ryggsteinen ridge area, northern North Sea. *AAPG Bulletin*, **104**, 1531–1565, https://doi.org/10.1306/03172018173

Ziegler, P. 1982. Triassic rifts and facies patterns in Western and Central Europe. *International Journal of Earth Sciences*, **71**, 747–772, https://doi.org/10.1007/BF01821101

Ziegler, P. 1990. Tectonic and palaeogeographic development of the North Sea rift system. *In:* Blundell, D.J. and Gibbs, A.D. (eds) *Tectonic Evolution of the North Sea Rifts*. Clarendon Press, Oxford, UK, 1–36.

Ziegler, W.H. 1975. Geologic evolution of North Sea and its tectonic framework. *AAPG Bulletin*, **59**, 1073–1097, https://doi.org/10.1306/83D91F2E-16C7-11D7-8645000102C1865D